Gondwana Research 22 (2012) 325–340

Contents lists available at SciVerse ScienceDirect

Gondwana Research

journal homepage: www.elsevier.com/locate/gr

Late Paleozoic calc-alkaline to shoshonitic magmatism and its geodynamic implications, Yuximolegai area, western Tianshan, Xinjiang

Wu-Bin Yang [a,b], He-Cai Niu [a,c,*], Qiang Shan [a], Yong Luo [d], Wei-Dong Sun [a], Cong-Ying Li [a,b], Ning-Bo Li [a,b], Xue-Yuan Yu [a]

[a] Key Laboratory of Mineralogy and Metallogeny, Guangzhou Institute of Geochemistry, Chinese Academy of Sciences, Guangzhou 510640, PR China
[b] Graduate University of Chinese Academy of Sciences, Beijing 100049, PR China
[c] Xinjiang Research Center for Mineral Resources, Chinese Academy of Sciences, Urumuqi 830011, PR China
[d] School of Environmental Science and Tourism, Nanyang Normal University, Nanyang 473061, PR China

ARTICLE INFO

Article history:
Received 8 June 2011
Received in revised form 15 October 2011
Accepted 15 October 2011
Available online 28 October 2011

Editor: R. Goldfarb

Keywords:
Western Tianshan
Calc-alkaline magmatism
Shoshonitic series
Post-subduction
Geodynamic evolution

ABSTRACT

Continuous Late Paleozoic magmatic activity in the western Tianshan, Xinjiang, China, temporally overlapped the Late Carboniferous collision between the Tarim and the Kazakhstan–Yili plates. Isotopic dating, whole-rock geochemistry, and isotopic characteristics of a suite of calc-alkaline to shoshonitic rocks from Yuximolegai area, in the eastern end of the Awulale Mountains, help define the tectonic evolution of this part of the Tianshan. Zircon U–Pb ages of a quartz diorite and a quartz syenite porphyry are 310.8 ± 2.1 Ma and 284.4 ± 3.6 Ma, respectively. The geochemical and isotopic characteristics of Late Carboniferous igneous rocks, including the quartz diorite, as well as basaltic andesite and K-rich trachyandesite, indicate an evolution from calc-alkaline towards shoshonitic series. This was generated by the partial melting of the hydrated mantle wedge induced by changing subduction angles. The younger quartz syenite porphyry, however, was more likely derived from the partial melting of a thickened crust in a post-collisional setting or the partial melting of hot juvenile basalt in the lower crust during Early Permian delamination of the subcontinental lithospheric mantle. Therefore, the generation of the calc-alkaline to shoshonitic igneous rocks in Yuximolegai area is genetically linked to the geodynamic evolution of the western Tianshan from convergent subduction to collision during the Late Paleozoic.

1. Introduction

Shoshonitic rocks are widely distributed in many orogenic belts (Blatter et al., 2001; Seghedi et al., 2004; Altunkaynak and Dilek, 2006; Chen et al., 2010; Eyuboglu et al., 2011). The formation of these magmatic rocks is controversial. There are various proposed models for their origins, which include asthenospheric upwelling induced by slab break-off (Koprubasi and Aldanmaz, 2004; Boztug et al., 2006; Altunkaynak, 2007; Altunkaynak and Genc, 2008; Negrete-Aranda and Canon-Tapia, 2008), lithospheric mantle delamination (Aldanmaz et al., 2000), and partial convective removal of the subcontinental lithospheric mantle (Altunkaynak and Dilek, 2006; Dilek and Altunkaynak, 2007). It is generally accepted that partial melting of subducted sediments could produce vein networks of clinopyroxene, amphibole, and phlogopite within the sub-continental lithospheric mantle (Foley, 1992; Gao et al., 2009). Interaction between these metasomatic veins and mantle magmas will result in the formation of shoshonites and high-K calc-alkaline rocks (Avanzinelli et al., 2009; Conticelli et al., 2009a,b). This genetic model is accepted for the formation of shoshonitic rocks associated with ultrapotassic, high-K calc-alkaline, or even calc-alkaline magmas (Muller et al., 1992; Blatter et al., 2003; Bonin, 2004; Callegari et al., 2004; Gill et al., 2004; Duggen et al., 2005).

In addition to tectonic implications, shoshonitic rocks have been reported to be the causative bodies for deposition of many important epithermal Au deposits and porphyry Cu–Au deposits, such as the Ladolam, Lihir, and Porgera Au deposits in Papua New Guinea (Muller and Groves, 1993; Muller et al., 2001); Bingham porphyry Cu–Mo–Au deposit in Utah, USA; Cripple Creek Au deposit in Colorado, USA; Cadia and Goonumblla porphyry Cu–Au deposits in New South Wales, Australia (Muller and Groves, 1993); Grasberg porphyry Cu–Au deposit in Indonesia (Muller and Groves, 1997); and Yulong porphyry Cu deposit in southwestern China (Jiang et al., 2006; Liang et al., 2006, 2009a,b; Hou et al., 2007). Therefore, a systematic study on shoshonitic rocks is essential for understanding the generation and distribution of associated epithermal and porphyry deposits.

The Awulale Mountains are located in the southwestern Central Asia Orogenic Belt. They include numerous Late Paleozoic volcanic and intrusive rocks and associated Cu (Au) deposits (Hong et al., 2003; Shan et al., 2009; Xiao and Kusky, 2009; Xiao et al., 2009; Luo et al., 2010). The tectonic setting of this region in the Late Paleozoic

* Corresponding author. Tel.: +86 20 85290906; fax: +86 20 85290130.
E-mail address: niuhc@gig.ac.cn (H.-C. Niu).

1342-937X/$ – see front matter © 2011 International Association for Gondwana Research. Published by Elsevier B.V. All rights reserved.
doi:10.1016/j.gr.2011.10.008

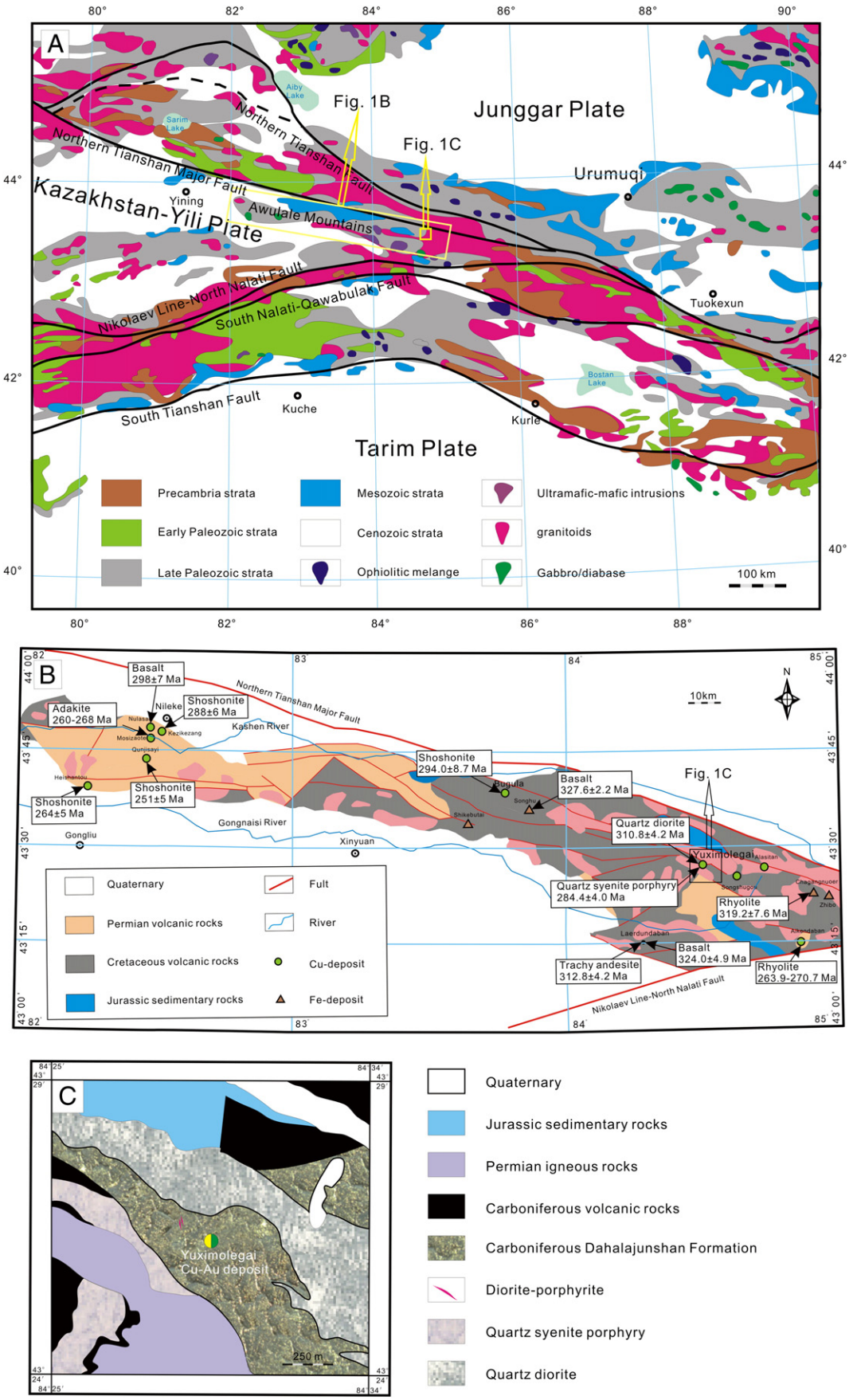

Fig. 1. (A) Tectonic sketch map of the western Tianshan (modified from Gao et al., 2009); (B) tectonic–geological sketch map of the Awulale Mountains (modified from Zhao et al., 2000); and (C) simplified geologic map of the Yuximolegai area. The labeled geochronological data in Fig. 1B are from references (Li et al., 1997; Chen et al., 2004b; Zhao et al., 2009; Zhu et al., 2009), this study and authors' unpublished data. The GPS position of the Yuximolegai porphyry Cu–Au deposit is: 84°23′28″ E, 43°24′30″ N.

Table 1
Major and trace element compositions of the Late Paleozoic igneous rocks in Yuximolegai. QD — quartz diorite, BA — basaltic andesite, KTA — K-rich trachyandesite, and QSP — quartz syenite porphyry.

Rock	QD	QD	QD	QD	QD	QD	QD	QD	QD	QD	QD	QD	BA	BA
Sample	YX08G-1	YX08G-2	YX08G-3	YX08G-4	YX08G-5	YX08G-6	YX8-1	YX8-2	YX8-3	YX8-4	YX8-5	YX8-7	YXAn-8	YX2-2
SiO_2	59.6	59.3	59.9	59.8	57.1	59.6	59.0	60.0	59.6	59.8	59.1	59.5	53.9	53.8
TiO_2	0.75	0.76	0.79	0.77	0.85	0.82	0.76	0.75	0.70	0.74	0.74	0.70	0.92	1.00
Al_2O_3	16.8	16.6	16.5	16.5	16.7	16.8	16.4	16.5	16.4	16.6	16.3	16.5	16.7	15.8
Fe_2O_{3T}	7.05	7.20	7.19	7.17	8.51	7.25	7.14	6.73	6.97	6.95	7.05	7.07	9.01	9.71
MnO	0.12	0.12	0.12	0.12	0.14	0.12	0.15	0.15	0.15	0.14	0.14	0.14	0.19	0.32
MgO	2.86	2.92	2.82	2.92	3.55	2.79	3.11	2.87	3.05	2.85	3.07	2.97	4.7	4.09
CaO	6.17	5.99	5.92	6.07	6.91	5.72	6.57	6.15	6.51	6.35	5.98	6.55	7.97	9.75
Na_2O	3.46	3.50	3.50	3.48	3.22	3.69	3.47	3.58	3.46	3.59	3.90	3.45	3.11	3.27
K_2O	1.86	1.75	1.86	1.84	1.63	1.44	1.78	1.96	1.86	1.70	1.95	1.88	1.20	0.81
P_2O_5	0.13	0.14	0.14	0.14	0.15	0.15	0.14	0.13	0.14	0.12	0.12	0.12	0.13	0.31
L.O.I	0.83	1.44	0.91	0.79	0.94	1.37	1.37	1.17	1.02	1.16	1.48	1.10	1.99	1.13
Total	99.67	99.67	99.66	99.66	99.67	99.68	99.9	99.91	99.92	99.91	99.9	99.92	99.86	99.92
Sc	22.7	31.6	22.4	22.6	28.4	21.7	22.8	20.7	22.3	20.6	22.2	13.4	31.6	30.5
Ti	5082	6524	5625	5244	6403	5712	5132	4908	4648	4876	4847	4643	5652	6708
V	173	220	173	176	219	165	177	170	176	171	174	174	229	238
Cr	18.4	22.0	18.7	16.6	24.4	14.0	23.5	25.8	20.7	20.7	19.7	19.7	137	201
Mn	1089	1468	1145	1082	1374	1124	1146	1104	1110	1060	1085	900	1489	2524
Co	32.7	36.4	29.9	32.8	43.0	37.0	20.3	17.7	18.1	17.3	18.0	16.8	26.2	26.7
Ni	8.27	11.0	6.48	7.94	13.9	5.88	11.4	12.1	11.7	8.95	9.94	10.2	22.2	51.6
Cu	34.0	41.5	25.2	36.4	43.4	36.4	18.9	17.2	22.5	12.0	22.0	34.6	57.1	21.4
Zn	49.3	75.9	43.9	55.6	69.6	68.7	53.8	47.0	51.1	43.9	47.0	44.8	203	103
Ga	19.0	24.1	18.7	18.4	19.7	18.8	17.9	17.7	17.7	17.8	17.2	16.4	16.6	17.5
Ge	1.68	2.08	1.68	1.55	1.74	1.70	1.56	1.50	1.75	1.68	1.73	1.80	1.58	1.58
Rb	57.5	63.4	58.7	56.1	59.3	39.4	55.4	53.2	52.1	44.5	55.9	29.8	48.9	31.8
Sr	311	393	303	306	329	310	298	297	287	298	294	280	305	329
Y	24.1	31.7	22.5	23.9	24.3	23.3	24.3	22.1	24.6	21.6	23.4	24.2	23.7	23.7
Zr	97.7	125	92.3	89.5	73.7	106	118	161	109	154	110	99.6	114	129
Nb	5.34	6.49	5.66	5.24	5.42	5.29	4.51	4.61	4.34	4.37	4.41	4.48	3.54	4.28
Cs	/	/	/	/	/	/	1.30	1.43	1.21	1.03	0.60	0.44	0.81	0.88
Ba	386	488	407	412	246	400	350	409	365	366	412	300	239	114
La	14.6	18.5	15.2	14.8	14.4	15.8	13.5	13.1	13.9	13.1	12.7	10.3	10.0	12.2
Ce	31.8	41.2	33.3	32.2	31.5	33.3	29.6	28.8	31.1	28.2	28.2	29.1	22.3	27.1
Pr	4.44	5.79	4.59	4.65	4.48	4.71	3.93	3.78	4.14	3.72	3.80	3.39	3.22	3.72
Nd	19.3	25.2	18.9	19.6	19.0	19.9	17.3	16.2	17.7	16.0	16.7	15.0	14.2	16.9
Sm	4.34	5.89	4.25	4.37	4.46	4.46	3.91	3.6	4.04	3.56	3.88	3.64	3.52	3.99
Eu	1.16	1.52	1.11	1.17	1.16	1.27	1.14	1.11	1.08	1.12	1.07	1.03	1.05	1.18
Gd	4.21	5.63	4.00	4.27	4.39	4.29	4.28	3.92	4.31	3.85	4.05	4.10	3.90	4.44
Tb	0.75	0.95	0.69	0.75	0.71	0.72	0.79	0.70	0.77	0.70	0.75	0.75	0.77	0.80
Dy	4.56	6.17	4.43	4.68	4.54	4.38	4.74	4.3	4.74	4.18	4.53	4.66	4.63	4.69
Ho	0.95	1.28	0.92	0.99	0.99	0.95	0.96	0.86	0.96	0.86	0.93	0.98	0.94	0.96
Er	2.75	3.71	2.75	2.86	2.72	2.59	2.78	2.51	2.90	2.57	2.66	2.87	2.69	2.78
Tm	0.39	0.56	0.41	0.41	0.40	0.39	0.42	0.4	0.44	0.39	0.41	0.43	0.40	0.41
Yb	2.68	3.63	2.48	2.58	2.57	2.49	2.78	2.63	2.92	2.63	2.75	2.89	2.63	2.67
Lu	0.42	0.57	0.40	0.43	0.42	0.38	0.43	0.42	0.46	0.40	0.44	0.45	0.42	0.42
Hf	2.76	3.43	2.66	2.74	2.11	2.88	3.33	4.49	3.31	4.26	3.23	3.07	3.18	3.77
Ta	0.42	0.46	0.44	0.43	0.39	0.37	0.37	0.39	0.39	0.37	0.39	0.42	0.29	0.34
Pb	4.53	8.14	5.57	4.51	5.64	5.01	7.35	4.07	4.18	4.18	3.42	4.67	15.2	6.28
Th	5.21	6.10	5.44	4.66	6.51	4.76	4.40	4.40	4.61	4.23	5.84	3.78	3.41	5.33
U	1.53	1.51	1.41	1.29	1.13	1.03	1.35	1.15	1.37	1.10	1.40	1.45	1.04	1.26

BA	BA	BA	BA	BA	KTA	KTA	KTA	KTA	KTA	KTA	KTA	KTA	KTA	KTA
YX2-3	YX2-7	YX3-3	YX08-2	YX08K-1	BST08-1	BST08-2	BST08-3	BST08-4	BST-6	BST-6B	BST-11	ALSB-1	ALSB-2	YXAn-4
51.0	53.6	56.1	55.6	56.1	50.7	50.6	50.8	50.7	55.3	53.4	53.9	53.3	55.9	58.0
1.05	1.02	0.81	1.20	1.00	1.30	1.28	1.13	1.12	0.84	0.92	1.12	1.02	1.30	0.86
16.1	16.3	16.6	18.5	16.0	17.8	17.9	18.4	18.5	16.6	17.5	17.9	16.8	17.1	16.4
14.0	10.1	7.91	8.21	11.2	11.0	10.3	10.2	10.1	8.97	10.0	9.09	8.16	9.83	8.00
0.32	0.30	0.21	0.14	0.15	0.25	0.26	0.17	0.18	0.30	0.62	0.50	0.56	0.13	0.17
4.82	3.46	4.20	3.12	2.61	3.80	3.80	3.29	3.31	3.65	3.82	3.52	3.83	1.98	2.85
5.28	8.02	8.50	5.36	5.58	4.50	4.62	6.12	6.40	1.88	1.16	3.30	2.74	1.19	3.54
2.62	3.73	2.72	3.36	2.65	3.98	3.21	4.04	3.95	3.93	2.58	1.91	4.24	4.54	3.76
1.52	1.60	1.28	1.83	1.93	3.86	4.63	3.24	3.14	4.72	7.02	5.03	4.89	5.32	4.81
0.30	0.33	0.23	0.31	0.23	0.24	0.24	0.21	0.21	0.21	0.22	0.20	0.24	0.20	0.11
2.86	1.46	1.39	2.09	2.22	2.34	2.88	2.11	2.14	3.51	2.71	3.22	4.04	2.28	1.37
99.88	99.91	99.89	99.68	99.64	99.7	99.73	99.7	99.71	99.82	99.85	99.67	99.75	99.7	99.91
29.6	29.9	26.4	26.4	50.6	35.3	32.1	27.3	27.9	29.0	28.6	28.3	31.5	34.3	20.9
6996	6511	5485	7649	6635	8913	8120	6291	7010	5234	5816	6934	6582	8590	5217
267	259	223	274	280	371	340	258	283	249	250	312	342	265	147
219	237	129	248	248	33.1	27.6	29.5	31.9	4.68	4.43	27.0	55.2	56.0	10.7
2571	2270	1633	1239	1359	2321	2412	1628	1689	2128	4688	3103	5399	1301	1269
40.6	24.6	22.7	82.1	56.8	29.7	27.3	35.1	33.9	24.0	21.2	22.2	33.2	54.5	18.4
62.2	54.1	32.4	114	71.0	29.2	28.1	31.9	32.3	1.41	3.51	22.6	24.3	12.1	5.58

(continued on next page)

Table 1 (*continued*)

BA	BA	BA	BA	BA	KTA	KTA	KTA	KTA	KTA	KTA	KTA	KTA	KTA	KTA
YX2-3	YX2-7	YX3-3	YX08-2	YX08K-1	BST08-1	BST08-2	BST08-3	BST08-4	BST-6	BST-6B	BST-11	ALSB-1	ALSB-2	YXAn-4
132	76.5	7.90	20.4	2924	190	88.4	206	168	4.12	31.3	176	905	7.25	9.88
279	124	93.5	126	110	242	236	110	133	210	362	460	900	426	84.6
19.4	17.7	17.6	19.9	19.0	21.3	19.6	19.8	21.2	17.8	18.9	14.9	19.5	19.3	15.6
1.99	1.25	1.49	1.86	3.30	1.59	1.36	1.50	1.64	1.51	1.19	0.92	1.69	2.22	1.16
60.2	79.9	54.2	84.2	92.5	214	243	160	168	181	325	230	261	233	129
268	302	384	213	196	380	340	305	330	94.2	167	267	264	175	234
21.9	22.1	20.2	19.8	16.8	33.5	32.2	26.8	28.2	23.7	27.0	27.6	23.4	35.3	17.2
135	131	131	158	126	154	142	123	121	115	131	120	128	188	91.2
4.39	4.25	3.97	5.69	4.69	4.89	4.76	4.08	4.05	3.37	3.91	3.74	3.78	5.69	3.24
2.15	1.02	1.28	/	/	/	/	/	/	2.67	3.40	1.62	/	/	1.74
404	206	284	226	158	783	1065	331	337	743	1592	1685	931	1542	944
13.1	11.8	10.8	16.9	13.2	14.0	13.5	10.2	10.4	21.3	13.2	10.2	9.60	12.8	8.64
28.5	25.2	24.2	36.0	32.0	32.1	29.9	24.5	27.2	44.9	29.7	25.3	22.8	32.1	18.9
3.77	3.51	3.29	5.00	4.51	4.93	4.56	3.79	3.97	5.89	4.03	3.68	3.39	4.96	2.52
17.0	15.7	14.5	20.7	19.4	22.0	21.0	17.4	18.5	24.9	17.9	17.6	15.0	22.7	10.7
3.89	3.76	3.27	4.54	4.41	5.59	5.37	4.53	4.70	5.12	4.17	4.55	3.74	5.90	2.63
0.85	1.05	0.98	1.18	1.03	1.63	1.46	1.30	1.35	1.25	0.97	1.07	1.08	1.83	0.69
4.15	4.03	3.63	4.11	3.81	5.88	5.75	4.72	5.11	4.76	4.85	5.21	4.07	6.54	2.94
0.71	0.75	0.66	0.63	0.63	1.02	0.97	0.83	0.88	0.78	0.87	0.94	0.71	1.12	0.54
4.21	4.37	3.95	3.99	3.77	6.07	6.16	4.83	5.48	4.56	5.37	5.64	4.79	6.69	3.38
0.87	0.91	0.83	0.83	0.75	1.32	1.33	1.09	1.13	0.94	1.10	1.16	0.98	1.38	0.67
2.47	2.64	2.33	2.18	2.07	3.75	3.72	2.92	3.07	2.76	3.12	3.29	2.97	3.76	2.00
0.36	0.39	0.36	0.33	0.32	0.52	0.55	0.43	0.43	0.40	0.47	0.48	0.41	0.54	0.30
2.44	2.58	2.30	2.19	2.05	3.48	3.54	2.68	2.90	2.65	3.23	3.27	2.74	3.54	2.10
0.41	0.40	0.36	0.32	0.33	0.57	0.55	0.43	0.46	0.44	0.51	0.54	0.41	0.55	0.35
3.91	3.73	3.76	4.15	3.59	4.31	4.13	3.23	3.46	3.33	4.01	3.73	3.38	4.98	2.85
0.35	0.35	0.36	0.43	0.32	0.36	0.33	0.28	0.29	0.32	0.36	0.31	0.29	0.49	0.32
6.44	5.64	4.14	7.17	5.18	14.9	15.8	9.25	9.92	10.6	4.67	87.8	103	29.4	9.56
5.00	5.01	5.39	6.12	5.76	4.31	4.37	3.21	3.18	4.07	4.93	3.39	3.03	5.08	4.88
1.39	1.25	1.43	2.86	2.22	1.48	1.35	0.97	1.08	1.27	1.50	1.13	0.81	1.83	1.15

KTA	KTA	KTA	KTA	KTA	KTA	KTA	KTA	KTA	QSP	QSP	QSP	QSP	QSP	QSP
YX2-5	YX2-6	YX08-1	YX6-13	YXAn-6	YX2-1	YX6-2	YX08-4	BST-3B	YXQ-1	YXQ-2	YXQ-3	YXQ-4	YXQ-6	YXQ-7
52.6	53.7	47.9	53.1	56.8	52.1	54.7	58.6	54.6	59.7	62.1	58.8	59.3	59.0	61.9
1.04	1.04	1.04	0.54	0.95	1.00	0.87	0.85	0.86	1.20	1.02	1.16	1.16	1.16	1.02
16.0	16.2	17.4	15.3	16.7	15.4	18.3	17.0	16.6	17.1	15.5	16.7	16.7	16.6	15.6
9.49	9.84	15.3	14.0	7.58	10.9	7.41	6.80	11.0	8.15	6.26	8.35	8.10	8.17	6.59
0.38	0.30	0.27	0.28	0.21	0.42	0.22	0.22	0.24	0.10	0.14	0.07	0.08	0.07	0.14
4.40	3.22	3.88	2.09	3.69	4.33	4.26	3.15	4.29	0.22	1.30	0.18	0.16	0.18	1.25
7.47	7.57	6.88	8.24	4.10	8.95	3.38	4.52	2.57	1.10	1.73	1.20	1.16	1.21	1.90
3.49	3.13	2.61	0.09	4.94	2.91	5.85	3.72	4.24	4.79	3.98	4.40	5.03	4.55	4.71
3.23	3.22	2.52	4.47	3.09	2.30	2.76	3.48	2.62	6.34	6.54	7.88	6.99	7.69	5.41
0.31	0.34	0.35	0.04	0.12	0.32	0.11	0.12	0.11	0.60	0.34	0.61	0.60	0.62	0.36
1.48	1.33	1.64	2.37	1.68	1.26	2.12	1.24	2.78	0.39	0.75	0.33	0.32	0.34	0.84
99.9	99.9	99.68	100.6	99.9	99.91	99.88	99.66	99.86	99.69	99.66	99.67	99.67	99.66	99.67
29.9	30.8	30.4	46.4	24.8	29.0	20.8	21.0	28.3	18.5	14.1	19.8	20.3	19.0	16.2
6773	6889	6665	3425	5784	6554	5678	5617	5578	6376	6130	7728	7008	6254	6633
232	260	244	225	209	238	214	209	272	106	61.2	112	92.5	87.0	77.1
228	226	207	12.4	15.6	205	44.3	13.0	5.51	2.57	0.16	4.75	3.04	1.54	1.69
2808	2329	2374	1635	1553	3156	1529	1969	1790	947	1319	678	810	672	1395
28.9	27.5	103	152	22.3	26.6	25.9	26.8	19.5	22.4	25.6	20.1	19.8	37.5	36.9
72.0	57.7	153	30.4	6.80	55.3	25.0	6.37	2.38	2.83	1.43	3.68	2.53	2.60	4.21
96.9	43.1	142	3645	6.87	20.1	8.70	4.01	5.00	179	42.5	75.8	69.1	76.6	43.0
129	131	143	63.1	86.2	118	109	94.4	166	48.0	119	39.8	41.4	34.4	99.9
17.5	18.3	23.6	27.5	16.5	17.2	21.5	18.7	18.9	18.9	19.0	17.4	16.4	16.2	19.7
1.70	1.40	3.78	2.76	1.25	1.64	1.56	1.51	1.46	1.09	1.66	1.13	1.08	1.12	1.73
101	108	103	112	102	84.5	131	130	81.5	212	267	260	220	243	235
280	319	183	608	283	291	215	291	251	104	227	91.9	101	93.0	212
26.0	22.8	36.6	17.9	18.4	21.4	22.9	19.9	25.0	31.9	34.9	33.8	33.3	32.5	36.3
132	135	149	64.3	84.0	124	124	106	118	291	256	271	313	254	262
4.57	4.42	5.07	2.29	3.09	3.91	3.83	3.92	3.61	12.4	14.8	13.6	13.1	12.6	14.9
0.67	1.37	/	0.50	0.98	0.47	2.22	/	1.06	/	/	/	/	/	/
685	617	369	584	546	352	358	567	403	722	589	954	808	922	503
14.2	15.0	13.5	8.66	9.14	13.4	21.5	10.5	13.1	34.4	35.1	50.7	35.7	39.6	36.3
33.1	31.2	33.9	17.5	19.8	29.6	44.6	22.5	28.8	84.1	79.4	111	82.2	86.7	80.1
4.59	4.24	5.55	2.23	2.69	3.94	5.61	3.18	3.80	10.2	11.0	13.9	10.6	11.4	11.4
20.6	18.8	25.1	9.80	11.5	17.4	23.2	13.7	16.3	41.6	44.2	54.8	42.8	46.5	46.5
4.82	4.22	6.26	2.28	2.82	3.86	4.83	3.33	3.74	8.56	8.90	10.4	8.60	9.64	9.45
1.24	1.10	1.63	0.79	0.91	1.02	1.61	1.02	1.04	1.68	1.55	1.82	1.59	1.73	1.67
5.06	4.53	6.29	2.93	3.10	3.98	5.00	3.31	4.20	7.68	7.91	8.96	8.03	8.40	8.03
0.91	0.79	1.10	0.55	0.59	0.68	0.85	0.58	0.77	1.10	1.22	1.28	1.17	1.16	1.25
5.30	4.49	6.71	3.50	3.50	4.11	4.84	3.75	4.81	6.22	6.81	6.78	6.47	6.64	7.35
1.05	0.92	1.45	0.70	0.72	0.83	0.94	0.80	0.97	1.27	1.40	1.33	1.33	1.31	1.52

Table 1 (*continued*)

KTA	KTA	KTA	KTA	KTA	KTA	KTA	KTA	KTA	QSP	QSP	QSP	QSP	QSP	QSP
YX2-5	YX2-6	YX08-1	YX6-13	YXAn-6	YX2-1	YX6-2	YX08-4	BST-3B	YXQ-1	YXQ-2	YXQ-3	YXQ-4	YXQ-6	YXQ-7
2.96	2.65	4.27	2.03	2.11	2.42	2.61	2.14	2.85	3.50	4.08	3.74	3.71	3.70	4.38
0.44	0.40	0.62	0.30	0.31	0.37	0.39	0.31	0.42	0.50	0.62	0.53	0.53	0.54	0.64
2.91	2.60	4.28	1.90	2.12	2.44	2.64	2.18	2.75	3.51	3.96	3.43	3.69	3.42	4.02
0.45	0.41	0.71	0.29	0.35	0.38	0.43	0.34	0.45	0.54	0.65	0.53	0.59	0.53	0.68
3.91	3.88	3.84	1.94	2.53	3.57	3.78	2.96	3.41	7.65	6.88	7.22	8.05	6.90	7.27
0.36	0.37	0.38	0.23	0.27	0.33	0.40	0.38	0.32	0.82	1.00	0.98	0.94	0.87	1.07
5.05	7.17	7.82	29.8	3.48	6.19	3.27	8.78	5.61	9.81	19.2	9.68	11.4	7.96	14.1
5.22	4.85	4.70	2.64	4.05	4.54	6.31	5.37	4.25	23.8	22.4	25.7	23.8	24.6	20.8
1.51	1.15	2.72	1.60	1.00	1.09	1.96	1.47	1.15	4.44	4.89	5.18	4.59	4.95	4.48

is still debated. Some researchers suggest that the Carboniferous and Permian magmatic activity in the western Tianshan reflects intraplate magmatism (Che et al., 1996; Xia et al., 2002; Xia et al., 2004; Zuo et al., 2008; Su et al., 2011). Others propose that magmatic activity in the Carboniferous was subduction-related, whereas only the Permian magmatism was intraplate (Jiang et al., 1995; Jiang et al., 1996; Chen et al., 2004a,b; Zhu et al., 2006a,b; Gao et al., 2009; Zhu et al., 2009; Ren et al., 2011). Main arguments focus on the timing of geodynamic transformation and thus the overall tectonic setting of the western Tianshan in Late Paleozoic. Therefore, Niu et al. (2010) carried out a detailed geochemical study of quartz diorite from the Yuximolegai area (Fig. 1), and proposed that the quartz diorite and its associated basaltic andesite might be co-magmatic products of island arc development along a Late Carboniferous active continental margin. In this present study, ages, whole-rock geochemistry, and isotopic characteristics of a series of rocks in the Yuximolegai region in the eastern Awulale Mountains, from calc-alkaline to shoshonitic, including quartz diorite, basaltic andesite, K-rich trachyandesite, and quartz syenite porphyry, have been determined. We attempt to better define the genesis of the Late Paleozoic calc-alkaline to shoshonitic magmatism in the western Tianshan and to reconstruct the corresponding geodynamic evolution of the region.

2. Local geology

The rocks that outcrop in the Yuximolegai region include those of the Carboniferous Dahalajunshan, Akeshake, and Yishenjilike Formations, the Permian Tiemulike Formation, and the Early Jurassic Badaowan Formation. They are dominantly volcanic rocks (Fig. 1).

The Dahalajunshan Formation is composed of a suite of volcanic rocks, including rhyolite, trachyte, trachyandesite, and ignimbrite. The rocks are distributed mainly in the center of the study area (Fig. 1C), are NW-trending, and have a thickness of 7500–9000 m (Zhu et al., 2006b). The lower part of the formation is dominated by andesite breccia, dacitic tuff, ignimbrite, and basaltic andesite. Its upper part is composed of thick andesitic tuff breccia, dacitic tuff, dacite, and K-rich trachyandesite. The Akeshake Formation is composed of purple tuff, andesite, volcanic breccia, silty shale, grayish-green limestone, and grayish-green marl. It outcrops in the northeastern part of the study area. The Yishenjilike Formation is dominated by felsic volcanic rocks and these are intruded by a quartz syenite porphyry. There are angular unconformities between rocks of the Yishenjilike Formation and those of the underlying Early Carboniferous Akeshake Formation, as well as between the Yishenjilike Formation units and the overlying rocks of the Late Permian Tiemulike Formation. The Tiemulike Formation is composed of orogenic molasse, which is more than 1000 m in thickness. Its lower part is composed of conglomerate and coarse to medium grained feldspathic lithic sandstone, whereas its upper part is composed of medium to fine grained feldspathic sandstone and muddy siltstone. The 750-m-thick, Early Jurassic Badaowan Formation is composed of gray polymictic conglomerate, light gray coarse-grained lithic sandstone with gray black shale, and several thin coal layers. The Quaternary is dominated by alluvial gravel.

This study focuses on the calc-alkaline to shoshonitic igneous rocks of the Yuximolegai area. These include quartz diorite, basaltic andesite, and the shoshonitic rocks, including K-rich trachyandesite, intruding and as parts of the Dahalajunshan Formation, and the quartz syenite porphyry intrusion.

Quartz diorite, which intruded rocks in the lower part of the Dahalajunshan Formation, is mainly composed of feldspar, hornblende, and a small amount of quartz and biotite. It is generally gray, with subhedral to anhedral granular texture. The feldspar consists of mainly plagioclase and minor K-feldspar. The subhedral plagioclase is generally large (1×2 mm–2×3 mm) with twins. The xenomorphic K-feldspar occurs between the grains of plagioclase or hornblende, and is obviously later as suggested by its smaller grain sizes. The quartz diroite also contains 15%–20% subhedral–anhedral amphibole, 5%–7% anhedral

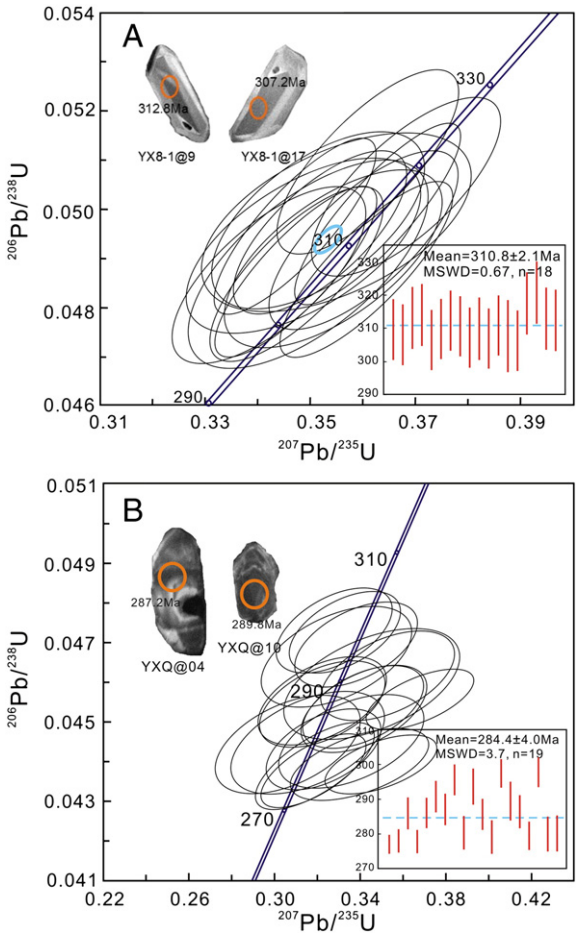

Fig. 2. Representative CL imagines of zircons and concordia diagrams for the quartz diorite (A) and quartz syenite porphyry (B). Zircon grains from quartz diorite were analyzed by SIMS (Niu et al., 2010), whereas zircon grains from quartz syenite porphyry were analyzed by LA–ICPMS.

quartz, and 5%–8% biotite. The grain size of amphibole is significantly smaller than that of plagioclase, but greater than that of K-feldspar. The K-feldspar is also typically spatially associated with biotite that occurs as rims on hornblende or between plagioclase grains. The major secondary minerals are sericite and chlorite.

Basaltic andesite of the Dahalajunshan formation is composed of 15% to 20% phenocrysts (0.1×0.1 to 0.3×0.6 mm^2) and 80% to 85% matrix. It has typical porphyritic texture. Phenocrysts are composed of plagioclase and hornblende, with minor pyroxene and magnetite. The matrix is composed mainly of plagioclase, hornblende, magnetite, and rare pyroxene, with a typical intergranular texture. The secondary minerals are sericite and chlorite.

The porphyritic K-rich trachyandesite is composed of 20% to 25% phenocrysts (0.2×0.2 to 0.4×0.6 mm^2) and 75% to 80% matrix. Phenocrysts are mainly composed of euhedral to semi-euhedral plagioclase and amphibole, with occasional pyroxene. The matrix is mainly composed of plagioclase, hornblende, alkali feldspar, and minor magnetite, with an intergranular texture. Secondary minerals are sericite and chlorite. The trachyandesite in the upper part of the Dahalajunshan Formation was deposited slightly later than the basaltic andesite.

Quartz syenite porphyry is composed of about 5% phenocrysts and about 95% matrix. Phenocrysts consist of orthoclase and plagioclase (An<30). The matrix is dominated by alkali feldspar, with 8% to 10% quartz and about 8% magnetite. Graphic texture results from associated alkali feldspar and quartz. Plagioclase and orthoclase in this rock are euhedral to semi-euhedral, whereas quartz and magnetite are mostly xenomorphic.

3. Analytical techniques

3.1. Zircon U–Pb dating

Zircons were first separated from samples using standard density and magnetic separation techniques, and secondly were hand-picked under a binocular microscope. Representative zircon grains were casted in an epoxy mount, and then were polished to near half sections to expose the internal structure for analysis. Polished zircons in epoxy mount were documented with transmitted and reflected light micrographs, as well as with cathodoluminescence (CL) images, to reveal their internal textures.

Zircon U–Pb dating of the quartz syenite porphyry was undertaken by using an Agilent 7500a ICP-MS coupled with a Resonetics RESOlution M-50 193 nm laser-ablation system at the Key Laboratory of Isotope Geochronology and Geochemistry at the Guangzhou Institute of Geochemistry, Chinese Academy of Sciences (GIGCAS). Details on operating conditions for the laser ablation system and the ICP-MS instrument and data processing are described by Liang et al. (2009a,b) and Tu et al. (2011). All analyses were carried out at an energy of 80 mJ, with a beam diameter of 31 μm and a repetition rate of 10 Hz. Helium was used as a carrier gas to enhance the transportation efficiency of the

Table 2
Zircon U–Th–Pb isotopes of the quartz diorite and the quartz syenite porphyry from Yuximolegai region.

Sample spots	Concentration and ratio			Isotopic ratios						Apparent ages (Ma)			
	U (ppm)	Th (ppm)	Th/U	$^{207}Pb/^{235}U$	±σ (%)	$^{206}Pb/^{238}U$	±σ (%)	$^{207}Pb/^{206}Pb$	±σ (%)	$^{207}Pb/^{235}U$	±σ	$^{206}Pb/^{238}U$	±σ
Quartzdiorite (CamercaIMS-1280)													
YX8-1@01	107	73.4	0.84	0.34860	2.6	0.04925	1.5	0.05134	2.1	303.7	6.9	309.9	4.6
YX8-1@02	212	227	1.18	0.34736	2.0	0.04868	1.5	0.05175	1.2	302.7	5.1	306.4	4.5
YX8-1@03	320	391	1.19	0.36268	1.8	0.04990	1.5	0.05271	1.0	314.2	4.8	313.9	4.6
YX8-1@04	141	108	0.96	0.35073	2.4	0.04975	1.5	0.05113	1.9	305.3	6.4	313.0	4.6
YX8-1@05	142	114	0.81	0.35457	2.4	0.04894	1.5	0.05254	1.8	308.2	6.3	308.0	4.6
YX8-1@06	144	120	0.95	0.35032	2.2	0.04919	1.5	0.05165	1.7	305.0	5.9	309.6	4.6
YX8-1@07	365	502	1.90	0.34711	1.8	0.04964	1.5	0.05071	1.0	302.5	4.7	312.3	4.6
YX8-1@08	383	512	1.47	0.35521	2.2	0.04965	1.5	0.05189	1.7	308.6	6.0	312.4	4.6
YX8-1@09	153	129	0.96	0.35490	2.9	0.04973	1.5	0.05176	2.5	308.4	7.9	312.8	4.6
YX8-1@10	242	229	1.21	0.36090	2.0	0.05096	1.5	0.05136	1.2	312.9	5.3	320.4	4.7
YX8-1@11	203	182	0.90	0.36823	2.0	0.05046	1.5	0.05293	1.3	318.3	5.4	317.3	4.6
YX8-1@12	185	168	1.12	0.34203	2.2	0.04867	1.5	0.05097	1.6	298.7	5.7	306.3	4.5
YX8-1@13	130	107	0.91	0.34955	2.7	0.04889	1.8	0.05186	2.0	304.4	7.1	307.7	5.4
YX8-1@14	127	104	0.98	0.35020	2.2	0.04938	1.5	0.05144	1.6	304.9	5.7	310.7	4.6
YX8-1@15	352	416	1.34	0.34678	1.8	0.04876	1.5	0.05159	0.9	302.3	4.6	306.9	4.5
YX8-1@16	262	312	1.49	0.34743	1.9	0.04923	1.6	0.05118	1.1	302.8	5.0	309.8	4.7
YX8-1@17	222	213	0.85	0.36059	1.8	0.04881	1.5	0.05358	1.1	312.7	5.0	307.2	4.5
YX8-1@18	137	111	0.79	0.35997	2.0	0.04935	1.5	0.05290	1.4	312.2	5.5	310.5	4.6
Quartzsyeniteporphyry (LA–ICPMS)													
YXQ@01	1237	841	0.68	0.5655	6.2	0.337	1.3	0.0433	0.06	294.9	10.2	273.5	3.4
YXQ@02	1012	692	0.68	0.5256	6.1	0.3144	1.7	0.0435	0.07	277.6	13.3	274.7	4.1
YXQ@03	1145	735	0.64	0.5488	6.3	0.342	1.9	0.0454	0.07	298.7	14.4	286.2	4.3
YXQ@04	1347	759	0.56	0.5567	6.2	0.3309	1.6	0.0433	0.06	290.3	12.0	273.3	3.7
YXQ@05	1483	1302	0.88	0.5895	6.4	0.3673	1.6	0.0454	0.06	317.7	11.7	286.3	3.7
YXQ@06	1266	611	0.48	0.5573	6.5	0.3528	2.0	0.0462	0.07	306.9	15.3	290.9	4.6
YXQ@07	955	614	0.64	0.5168	6.1	0.3223	2.0	0.0456	0.07	283.6	15.5	287.2	4.6
YXQ@08	1120	409	0.37	0.5259	5.9	0.3377	1.9	0.0469	0.07	295.4	14.3	295.7	4.4
YXQ@09	1127	955	0.85	0.5522	6.6	0.336	2.3	0.0445	0.08	294.2	17.1	280.6	4.9
YXQ@10	851	536	0.63	0.5159	6.2	0.3291	2.3	0.0467	0.08	288.9	17.7	293.9	5.2
YXQ@11	1620	974	0.60	0.5497	6.2	0.3407	1.9	0.0453	0.07	297.7	14.5	285.8	4.4
YXQ@12	1391	724	0.52	0.5268	6.3	0.3146	2.2	0.0437	0.08	277.7	16.8	275.6	4.9
YXQ@13	1239	957	0.77	0.5157	5.6	0.3327	1.7	0.0472	0.07	291.7	13.0	297.6	4.1
YXQ@14	917	490	0.53	0.5499	6.8	0.3453	2.7	0.046	0.09	301.2	20.3	289.8	5.7
YXQ@15	1386	1190	0.86	0.5189	5.9	0.322	1.9	0.0454	0.07	283.4	14.9	286.4	4.5
YXQ@16	1603	1787	1.11	0.5345	5.8	0.3233	1.8	0.0443	0.07	284.4	13.5	279.6	4.1
YXQ@17	1442	1229	0.85	0.5073	5.5	0.3275	1.8	0.0473	0.07	287.7	13.7	298.0	4.3
YXQ@18	1216	518	0.43	0.5053	6.0	0.3063	2.2	0.0444	0.08	271.3	17.4	280.2	5.1
YXQ@19	1020	537	0.53	0.5195	6.3	0.3152	2.4	0.0445	0.08	278.2	18.4	280.4	5.2

ablated material. A TEMORA 1 (417 Ma) sample was used as zircon standard (Black et al., 2003). Integration of background and analytical signals, and time-drift correction and quantitative calibration for trace elements, were undertaken by using the GLITTER 4.0 algorithm (Macquarie University). The analytical data were reduced, calculated, and plotted by using the Isoplot 3.0 programs of Ludwig (2003). Individual analyses in Table 1 and the concordia diagram (Fig. 2) are presented with 1σ error and uncertainties in weighted mean ages are quoted at 2σ (95% confidence level).

3.2. Whole-rock geochemistry analyses

Whole-rock samples were examined by optical microscopy. Unaltered or least-altered samples were selected for geochemical analysis. Both major and trace element compositions were analyzed in the State Key Laboratory of Isotope Geochemistry, GIGCAS. Major element oxides were determined by using the standard X-ray fluorescence method (Liang et al., 2009a,b). Trace elements were analyzed by inductively coupled plasma mass spectrometry, using a Perkin-Elmer Sciex ELAN 6000 instrument. Analytical procedures are the same as those described by Li (1997). About 50 mg of powdered sample were dissolved in high-pressure Teflon bombs with a $HF + HNO_3$ mixture. Rhodium was used as an internal standard to monitor signal drift during counting. Analytical precision for most elements is better than 3%.

For Sr–Nd isotope determination, sample powders were first spiked and dissolved in Teflon capsules with $HF + HNO_3$ acid. Secondly, Sr and REE were separated by using cation columns, and then Nd fractions were further separated by using HDEHP-coated Kef columns. Isotopic measurement was performed on the Micromass Isoprobe multicollector mass spectrometer at GIGCAS, following analytical procedures described by Wei et al. (2002) and Li et al. (2004). Measured $^{87}Sr/^{86}Sr$ and $^{143}Nd/^{144}Nd$ ratios were normalized to $^{86}Sr/^{88}Sr = 0.1194$ and $^{146}Nd/^{144}Nd = 0.7219$, respectively. The reported $^{87}Sr/^{86}Sr$ and $^{143}Nd/^{144}Nd$ ratios were respectively adjusted to the NBS SRM 987 standard with a $^{87}Sr/^{86}Sr$ value of 0.71025 and the Shin Etsu JNdi-1 standard with a $^{143}Nd/^{144}Nd$ value of 0.512115.

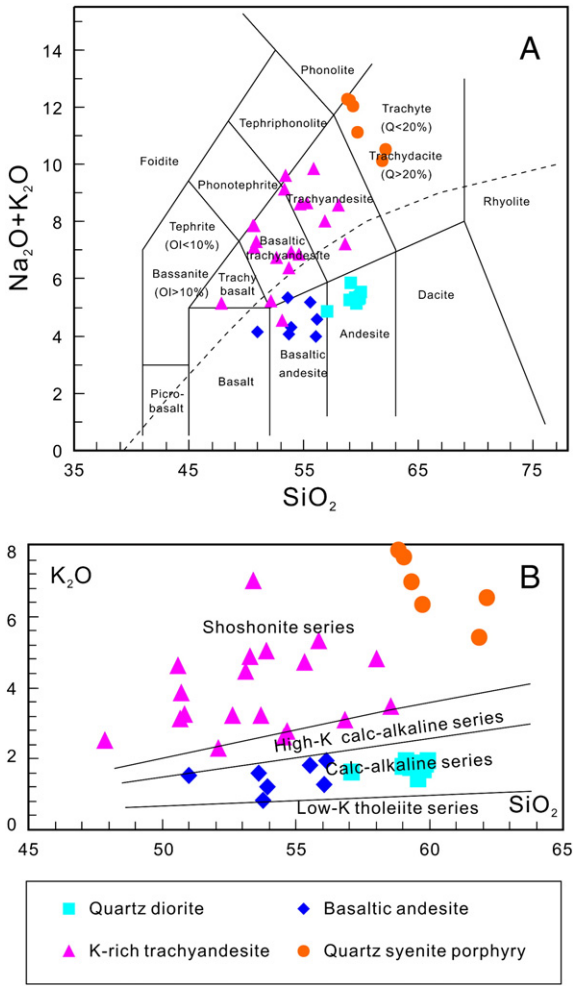

Fig. 3. TAS (A) and K_2O vs. SiO_2 (B) classification diagrams of the Late Paleozoic igneous rocks in Yuximolegai area (after Middlemost, 1994; Peccerillo and Taylor, 1976). The data for quartz diorite are from Niu et al. (2010)

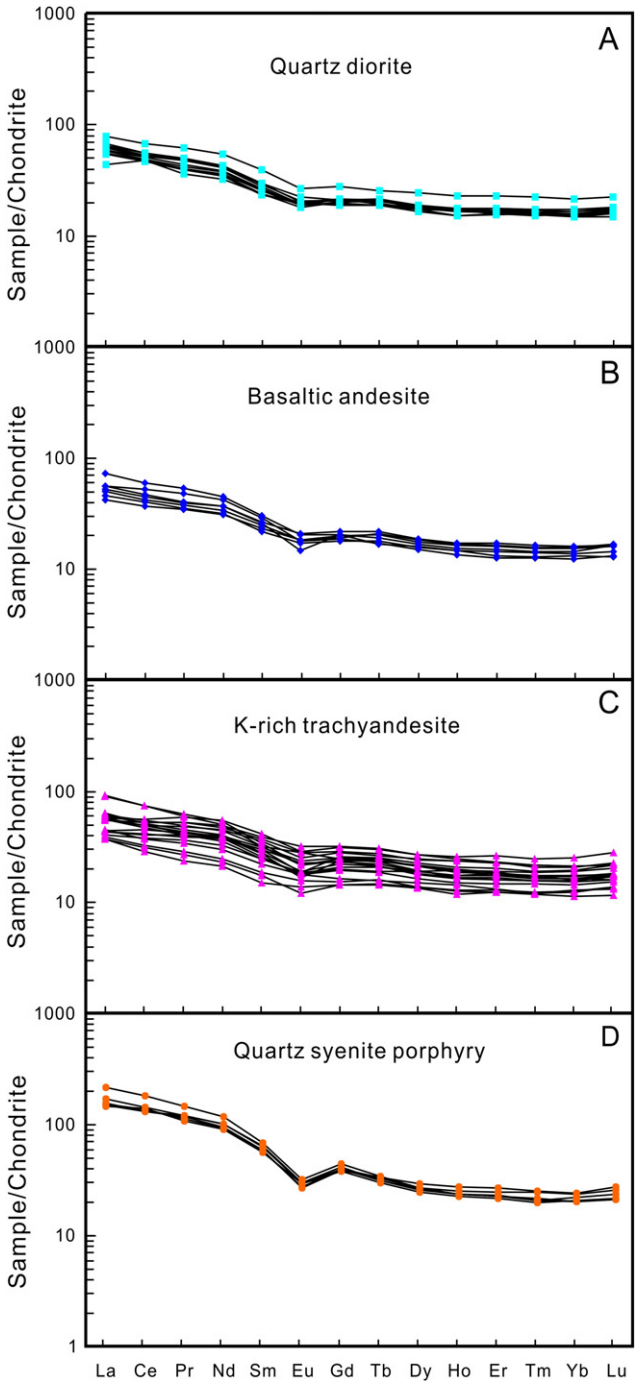

Fig. 4. REE distribution patterns for the Late Paleozoic igneous rocks in the Yuximolegai area. The data for quartz diorite are from Niu et al. (2010). The chondrite normalized data are from Sun and McDonough (1989).

4. Results

4.1. Zircon U–Pb geochronology

The zircon crystals from the quartz diorite are transparent, light olive brown and prismatic, and 150- to 200-μm-long and 40- to 60-μm-wide. They are typical magmatic zircons with clear oscillatory zoning in their CL imagines and high Th/U ratios. The contents of Th and U are 107–383 ppm and 73.4–512 ppm, respectively. The $^{206}Pb/^{238}U$ ages of the 18 analyses vary from 306 Ma to 320 Ma, with a weighted average value of 310.8 ± 2.1 Ma (Fig. 2A; Niu et al., 2010).

The zircon crystals from the quartz syenite porphyry are transparent, light brown and prismatic, with well developed prismatic face, and oscillatory zonation in their CL images. The Th and U contents of zircons from the quartz syenite porphyry, 409–1787 ppm and 851–1603 ppm, respectively, are much higher than those of the associated quartz diorite. The $^{206}Pb/^{238}U$ ages of the 19 analyses range from 273 Ma to 298 Ma, with a weighted average age of 284.4 ± 3.6 Ma (Fig. 2B).

4.2. Geochemistry of the Yuximolegai igneous suites

The major and trace elemental compositions of the Yuximolegai igneous rocks are listed in Table 2. Their SiO_2 contents vary from 47.9 wt.% to 62.1 wt.%. On a K_2O versus SiO_2 diagram (Fig. 3), they plot into two groups, calc-alkaline series (quartz diorite and basaltic andesite) and shoshonitic series (K-rich trachyandesite and quartz syenite porphyry). The limited range for the Ba/Rb ratio, combined with the large variation for the Ba/Nb ratio, indicate that both the calc-alkaline series and the K-rich shoshonitic series are not significantly affected by later alteration (Zhang and O'Reilly, 1997). This is also consistent with the petrographic observations of only weak sericitization of the feldspar and weak chloritization of the hornblende. Therefore, the analyses of both major and trace elements of the Yuximolegai igneous suite in this study can be interpreted as representative of the magma.

The major element compositions of quartz diorite samples are quite consistent (Table 2). They plot in quartz diorite field in the discrimination diagram of Middlemost (1994), with aluminous (Al_2O_3/Na_2O+K_2O ratios varying from 1.92 to 2.19 and $Al_2O_3/CaO+Na_2O+K_2O$ ratios varying from 0.83 to 0.93) and calc-alkaline features (CA/TH ratios of ~1.2). Their SiO_2, K_2O, and MgO contents vary from 57.1 wt.% to 60.0 wt.%, 1.44 wt.% to 1.96 wt.%, and 2.85 wt.% to 3.55 wt.%, respectively. Contents of compatible elements of Cr, Co, and Ni in quartz diorite vary from 14.0 ppm to 25.8 ppm, 17.7 ppm to 43.0 ppm, and 5.88 to 13.9 ppm, respectively. They are lower than those of the basaltic andesite from Dahalajunshan Formation. This could be caused by their high SiO_2 contents (Table 2). The large ion lithophile elements (LILE) of Rb, Ba, and Th in quartz diorite are enriched, with concentrations of 39.4–63.4 ppm, 246–488 ppm, and 4.2–6.5 ppm, respectively. Total rare earth element (REE) contents of the quartz diorite vary from 82.3 ppm to 121 ppm, with $(La/Sm)_N$ values from 1.83 to 2.38, $(La/Yb)_N$ values from 2.56 to 4.54, $(Dy/Yb)_N$ values from 1.06 to 1.21, and δEu values from 0.79 to 0.92. These show that there is minor REE fractionation and a slight Eu negative anomaly (Fig. 4A). Contents of the high field strength elements (HFSE) vary from 4.3 ppm to 6.5 ppm for Nb, 0.37 ppm to 0.46 ppm for Ta, and 4643 ppm to 6524 ppm for Ti (Table 2). These HFSE are relatively depleted as is shown in primary mantle normalized trace element spider diagram (Fig. 5A).

Contents of SiO_2 (51.0 wt.% to 56.1 wt.%) and total alkali (Na_2O+K_2O: 3.91 wt.% to 5.19 wt.%) of the basaltic andesite are lower than those of the associated quartz diorite in the TAS diagram (Fig. 3A). The major element geochemistry of this basaltic andesite shows that it is a typical calc-alkaline volcanic rock (Irvine and Baragar, 1971, see Fig. 3B). Concentrations Cr, Co, and Ni in basaltic andesite are 129–280 ppm, 24.6–82.1 ppm, and 22.2–114 ppm, respectively. They are

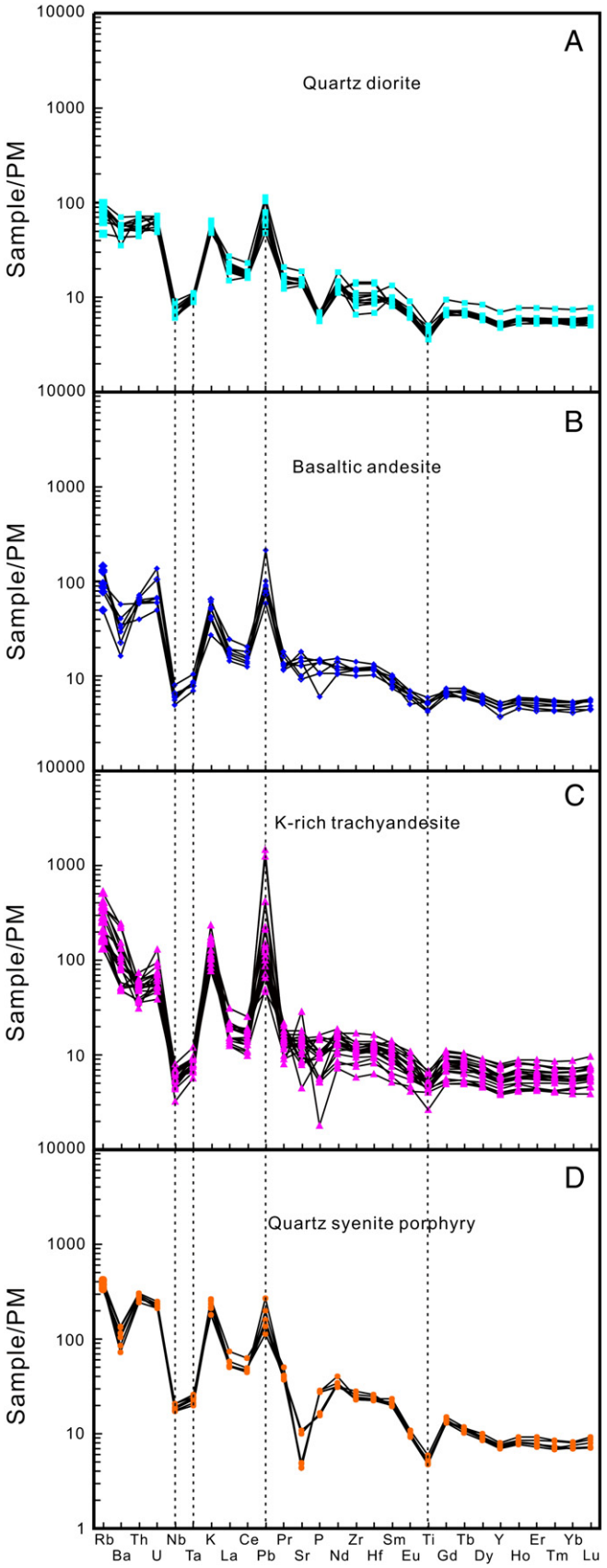

Fig. 5. Trace element spider diagrams of the Late Paleozoic igneous rocks in the Yuximolegai area.
The data for quartz diorite are from Niu et al. (2010). The primary mantle normalized data are from Sun and McDonough (1989).

much higher than those elements in the other three types of igneous rocks in the Yuximolegai region. Total REE concentrations of the basaltic andesite vary from 70.7 ppm to 98.9 ppm, with $(La/Sm)_N$, $(La/Yb)_N$, $(Dy/Yb)_N$, and δEu values varying from 1.82 to 2.40, 2.71 to 5.52, 1.13 to 1.23, and 0.53 to 0.76, respectively. These show that there is once again minor REE fractionation and a slight Eu negative anomaly (Fig. 4B). Relatively high concentrations of LILE (31.8 ppm to 84.2 ppm Rb, 114 ppm to 404 ppm Ba, and 1.04 ppm to 2.86 ppm U), together with depleted HFSE (3.54 ppm to 5.69 ppm Nb and 0.29 ppm to 0.42 ppm Ta), and remarkably enriched Pb (4.14 ppm to 15.8 ppm) of the basaltic andesite, as well as of the associated quartz diorite, are typical of collisional orogenesis (Altherr et al., 2008; Boari et al., 2009).

The K-rich trachyandesite contains variable contents of K_2O (2.62 wt.% to 7.02 wt.%), SiO_2 (47.9 wt.% to 58.6 wt.%), and total alkali ($Na_2O + K_2O$: 4.56 wt.% to 9.86 wt.%) (Fig. 3A). Compared to the above calc-alkaline rocks, the K-rich trachyandesite is enriched in K_2O and Na_2O, and depleted in CaO (1.16 wt.% to 8.95 wt.%) and TiO_2 (0.54 wt.% to 1.30 wt.%). Contents of its compatible elements are lower than of the basaltic andesite, with 4.43 ppm to 228 ppm Cr, 18.4 ppm to 151 ppm Co, and 1.41 ppm to 153 ppm Ni (Table 2). Its total content of REE varies from 56.4 ppm to 119 ppm, with $(La/Sm)_N$, $(La/Yb)_N$, $(Dy/Yb)_N$, and δEu values varying from 1.39 to 2.87, 2.24 to 5.83, 1.05 to 1.26, and 0.55 to 0.81, respectively. It has similar REE geochemical characteristics to the basaltic andesite. In addition, its contents of LILE and Pb are enriched, such that it is characterized by81.5 ppm to 325 ppm Rb, 331 ppm to 1685 ppm Ba, 94 ppm to 609 ppm Sr, and 3.27 ppm to 103 ppm Pb. However, its contents of HFSE are relatively depleted, with 2.29 ppm to 5.69 ppm Nb, 0.23 ppm to 0.49 ppm Ta, and 3425 ppm to 8913 ppm Ti (Fig. 5).

The quartz syenite porphyry has homogenous major oxides contents, including SiO_2, TiO_2, Al_2O_3, Fe_2O_{3T}, CaO, Na_2O, and K_2O, but with the exception of MgO that varies from 0.18 wt.% to 1.30 wt.% (Table 2). The quartz syenite porphyry has high abundances of silica and alkali elements, and is depleted in Ca and Ti, which typifies shoshonitic igneous rocks. The abundances of compatible elements are obviously lower than that in the other three types of associated ig-

Table 3
Sr–Nd isotopic data of the Late Paleozoic igneous rocks from Yuximolegai region.

Sample	Rb (ppm)	Sr (ppm)	Sm (ppm)	Nd (ppm)	$^{87}Rb/^{86}Sr$	$^{87}Sr/^{86}Sr$	2σ	$(^{87}Sr/^{86}Sr)_i$	εSr (T)	$^{147}Sm/^{144}Nd$	$^{143}Nd/^{144}Nd$	2σ	$(^{143}Nd/^{144}Nd)_i$	εNd (T)	$T_{DM,1}$ (Ma)	$T_{DM,2}$ (Ma)
Quartz diorite																
YX08G5	59.3	329	4.46	19.0	0.5225	0.707024	0.000005	0.704713	8.2	0.1416	0.512682	0.000008	0.512394	3.1	989	822
YX08G6	39.4	310	4.46	19.9	0.3673	0.706380	0.000007	0.704755	8.8	0.1355	0.512665	0.000007	0.512390	3.0	946	830
YX8-1	55.4	298	3.91	17.3	0.5372	0.706938	0.000013	0.704562	6.0	0.1368	0.512650	0.000010	0.512372	2.6	991	858
YX8-3	52.1	287	4.04	17. 7	0.5254	0.706751	0.000016	0.704427	4.1	0.1381	0.512662	0.000010	0.512382	2.8	983	843
YX8-4	44.5	298	3.56	16.0	0.4316	0.706475	0.000005	0.704566	6.1	0.1344	0.512689	0.000007	0.512416	3.5	886	788
YX8-5	55.9	294	3.88	16.7	0.5509	0.707219	0.000013	0.704783	9.1	0.1404	0.512697	0.000008	0.512412	3.4	943	795
YX8-7	29.8	280	3.64	15.0	0.3077	0.706784	0.000014	0.705423	18	0.1469	0.512652	0.000009	0.512354	2.3	1135	887
Basaltic andesite																
YXAn-8	48.9	305	3.52	14.2	0.4642	0.706846	0.000005	0.704759	8.9	0.1496	0.512728	0.000008	0.512419	3.7	1003	776
YX2-2	31.8	329	3.99	16.9	0.2799	0.705887	0.000017	0.704628	7.0	0.1427	0.512804	0.000008	0.512509	5.4	744	633
YX2-7	79.9	302	3.76	15.7	0.7652	0.707140	0.000017	0.703699	−6.2	0.1447	0.512782	0.000009	0.512483	4.9	813	675
YX3-3	54.2	384	3.27	14.5	0.4078	0.705920	0.000007	0.704086	−0.7	0.1362	0.512794	0.000007	0.512513	5.5	700	627
K-rich trachyandesite																
YX2-1	84.5	291	3.86	17.4	0.8413	0.708568	0.000018	0.704785	9.3	0.1342	0.512763	0.000009	0.512485	5.0	743	670
YX2-5	101	280	4.82	20.6	1.0427	0.709631	0.000017	0.704941	11	0.1411	0.512786	0.000009	0.512494	5.1	765	656
YX2-6	108	319	4.22	18.8	0.9821	0.708508	0.000014	0.704091	−0.6	0.1361	0.512791	0.000008	0.512510	5.4	705	632
Quartz syenite porphyry																
YXQ1	212	104	8.56	41.6	5.8969	0.730559	0.000005	0.705974	26	0.1244	0.512690	0.000008	0.512451	3.7	787	753
YXQ2	267	227	8.90	44.2	3.4015	0.719308	0.000006	0.705126	14	0.1217	0.512694	0.000008	0.512461	3.9	756	738
YXQ3	260	91.9	10.4	54.8	8.2080	0.740013	0.000006	0.705792	23	0.1151	0.512675	0.000010	0.512454	3.8	736	749
YXQ4	220	101	8.60	42.8	6.2994	0.732484	0.000004	0.706220	29	0.1215	0.512700	0.000006	0.512466	4.0	745	729
YXQ6	243	93.0	9.64	46.5	7.5730	0.735684	0.000007	0.704110	−0.7	0.1252	0.512681	0.000007	0.512441	3.5	809	770
YXQ7	235	212	9.45	46.5	3.2060	0.718619	0.000006	0.705252	16	0.1230	0.512700	0.000006	0.512464	4.0	757	733

The notation of ε_{Nd}, $f_{(Sm/Nd)}$ and T_{DM} are defined as: $\left(\frac{^{87}Sr}{^{86}Sr}\right)_i = \left(\frac{^{87}Sr}{^{86}Sr}\right)_{sample} - \left(^{87}Rb/^{86}Sr\right)_{sample}(e^{\lambda_1 t} - 1)$. The εNd (T) values were calculated using the present-day values for a chondritic uniform reservoir (CHUR) $^{143}Nd/^{144}Nd = 0.512638$ and $^{147}Sm/^{144}Nd = 0.1967$.

$$\varepsilon Nd(T) = \left[\frac{\left(^{143}Nd/^{144}Nd\right)^{T}_{sample}}{\left(^{143}Nd/^{144}Nd\right)^{T}_{CHUR} - 1}\right] \times 10^4 = \left[\left(^{143}Nd/^{144}Nd\right)_{sample} - \frac{\left(^{147}Sm/^{144}Nd\right)_{sample}\left(e^{\lambda_2 t} - 1\right)}{\left(^{143}Nd/^{144}Nd\right)^{0}_{CHUR} - \left(^{147}Sm/^{144}Nd\right)^{0}_{CHUR}\left(e^{\lambda_2 t} - 1\right) - 1}\right] \times 10^4$$

where $\left(\frac{^{87}Sr}{^{86}Sr}\right)_i$ is the initial value of sample, $(^{143}Nd/^{144}Nd)_{CHUR} = 0.512638$ and $(^{147}Sm/^{144}Nd)_{CHUR} = 0.1967$. The decay constants ($\lambda_1$ and λ_2) used in age calculations were 1.42×10^{-11} year^{-1} for ^{87}Rb (Steiger and Jäger, 1977) and 6.54×10^{-12} year^{-1} for ^{147}Sm (Lugmair and Marti, 1978).
Nd model ages were calculated in two ways (T_{DM} and $T_{DM,2}$). The one-stage model age (T_{DM}) was calculated assuming linear Nd isotopic growth of the depleted mantle reservoir from εNd = 0 at 4.56 Ga to εNd = +10 at present.

$$T_{DM} = \frac{1}{\lambda_2}\ln\left[1 + \left(^{143}Nd/^{144}Nd\right)_{DM} - \frac{\left(^{143}Nd/^{144}Nd\right)_{sample}}{\left(^{147}Sm/^{144}Nd\right)_{DM} - \left(^{147}Sm/^{144}Nd\right)_{sample}}\right], \quad f_{(Sm/Nd)} = \frac{\left(^{147}Sm/^{144}Nd\right)_{sample}}{\left(^{147}Sm/^{144}Nd\right)_{CHUR} - 1}$$

The two-stage model age, which is applied for samples with $^{147}Sm/^{144}Nd$ ratios larger than 0.14, or $f_{Sm/Nd}$ ratios of > -0.2 or < -0.6, was obtained assuming that the protolith of the granitoid magmas had a Sm/Nd ratio (or $f_{(Sm/Nd)}$) of the average continental crust (Keto and Jacobsen, 1987).
$T_{DM,2} = T_{DM} - \frac{(T_{DM} - t)(f_{cc} - f_{sample})}{f_{cc} - f_{DM}}$ where f_{cc}, $f_{sample}$and f_{DM} are $f_{(Sm/Nd)}$ values of the continental crust, the sample and the depleted mantle, respectively. In our calculation, $f_{cc} = -0.4$ and $f_{DM} = 0.08592$, and t is the emplacement age of the granite. The depleted mantle values $(^{143}Nd/^{144}Nd)_{DM}$ and $(^{147}Sm/^{144}Nd)_{DM}$ are 0.51315 and 0.21317.

neous rocks in the Yuximolegai region, with 0.16 ppm to 4.75 ppm Cr, 9.80 ppm to 36.9 ppm Co, and 1.43 ppm to 3.68 ppm Ni. These data are consistent with the absence of pyroxenes, hornblende, and other mafic minerals in the quartz syenite porphyry. The total REE concentration in the quartz syenite porphyry is significantly higher than that of the other three types of igneous rocks, ranging from 205 ppm to 269 ppm, with $(La/Sm)_N$ varying from 2.48 to 3.14, $(La/Yb)_N$ from 6.35 to 10.6, $(Dy/Yb)_N$ from 1.13 to1.32, and δEu from 0.44 to 0.50. This reflects REE fractionation and an Eu negative anomaly (Fig. 4D). The abundances of HFSE and Sr are depleted (Fig. 5D).

4.3. Sr–Nd isotopic data

The Sr and Nd isotopic compositions of selected samples are listed in the Table 3 and plotted in Fig. 6. The studied rocks have a small range of initial Sr isotope ratios (0.703699–0.706220) and have positive $\varepsilon_{Nd}(t)$ (at 300 Ma) values (2.3–5.5). Most of the analyses plot in the field of lithospheric mantle melting (Fig. 6). The quartz diorite has the lowest $\varepsilon_{Nd}(t)$ values (2.3–3.5), with small initial $^{87}Sr/^{86}Sr$ variation, compared to the other three types of igneous rocks in the studied area. Both the calc-alkaline series and shoshonitic series show Sr–Nd isotopic values characteristic of lithospheric mantle melting.

5. Petrogenesis of the Yuximilegai magmatic rocks

5.1. The calc-alkaline quartz diorite and basaltic andesite

Trace element patterns that are significantly depleted in Nb–Ta, Zr–Hf, and Ti, and enriched in Pb, are typical of subduction-related magmatism (Foley et al., 1987; Altherr et al., 2008; Boari et al., 2009), suggesting that both the quartz diorite and the basaltic andesite were generated at a convergent plate margin. The ratios of Th/Yb and Ta/Yb show characteristics of active continental margin arc igneous rocks (Fig. 7A), with Th/Yb = 1.31–2.53 and Ta/Yb = 0.13–0.15 for the quartz diorite, and Th/Yb = 1.29–2.81 and Ta/Yb = 0.11–0.19 for the basaltic andesite (Rottura et al., 1998). The Zr/Nb (26.8–32.9 and 13.6–35.3) and Nb/Th (0.74–1.04 and 0.83–1.19) ratios of quartz diorite and basaltic andesite also show characteristics of arc

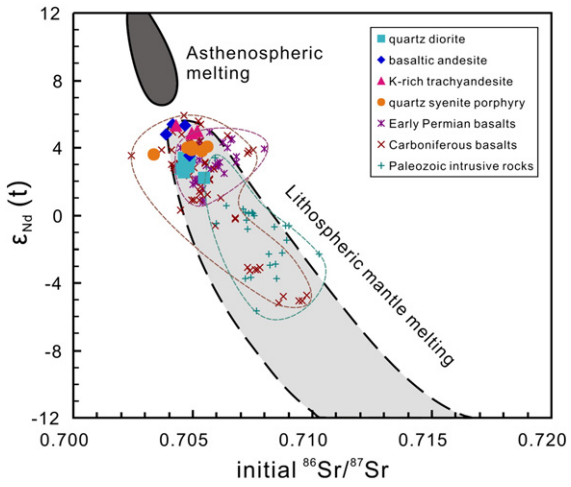

Fig. 6. Initial $^{87}Sr/^{86}Sr$ vs. $\varepsilon_{Nd}(t)$ diagram for the Late Paleozoic igneous rocks in the Yuximolegai area compared with Early Permian basalts (Xiong et al., 2001; Zhao et al., 2004, 2009; Luo et al., 2010), Carboniferous basalts (Ni et al., 1995; Qian et al., 2006; Zhu et al., 2006a, 2009; Wang et al., 2011), and Paleozoic intrusive rocks (Hu et al., 2008; Zhang et al., 2009; Tang et al., 2010; Zhang et al., 2010) from the western Tianshan. The field for asthenospheric melting is based on Nd and Sr isotopes from MORB, and the field for lithospheric mantle melting is from worldwide alkali basalts, kimberlites, and lamproites (Davies and Blanckenburg, 1995). Symbol size is larger than analytical error (2σ).

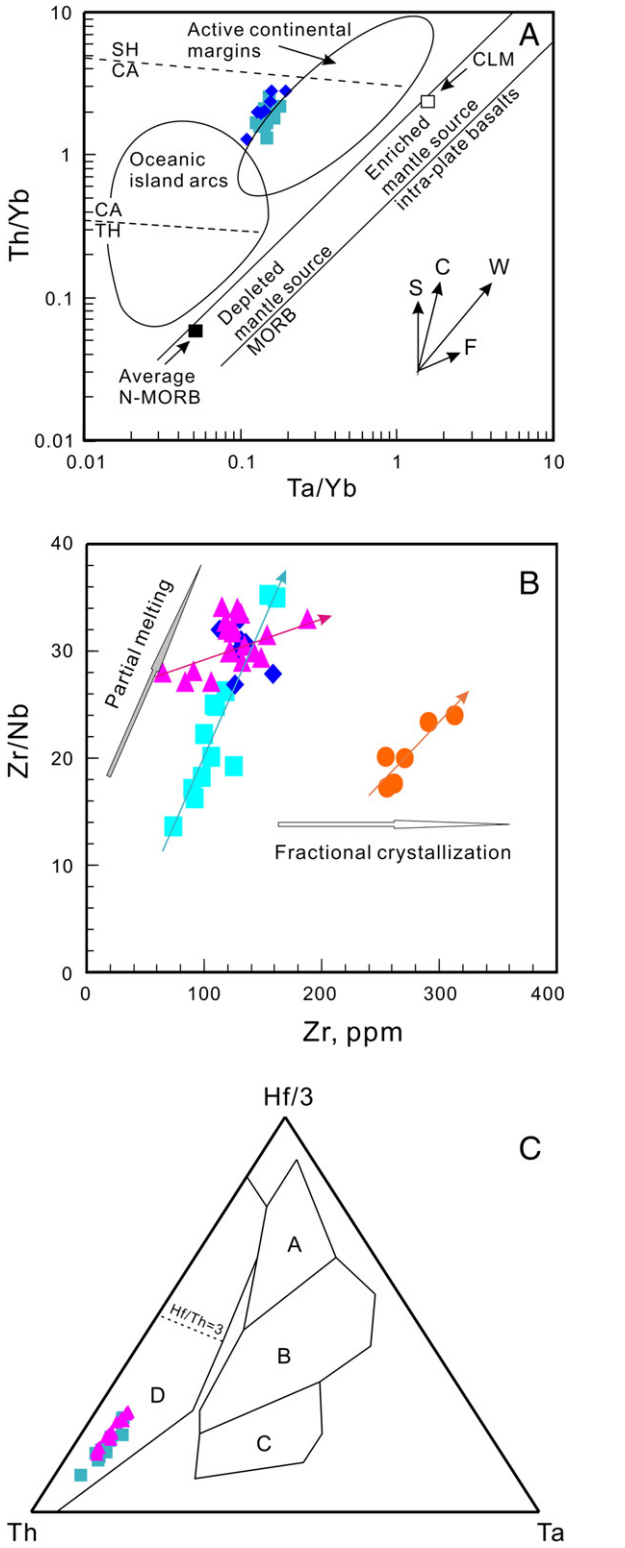

Fig. 7. Discrimination diagram for tectonic settings of the igneous suites in the Yuximolegai area. (A) Th/Yb vs. Ta/Yb diagram (Pearce, 1982), SH — shoshonitic basalt, CA — calc-alkaline basalts, TH — tholeiitic basalt; (B) Zr/Nb vs. Zr diagram (Geng et al., 2009), show the trends of partial melting and fractional crystallization; (C) Hf/3–Th–Ta discrimination diagram (Wood, 1980). A, N-type MORB; B, E-type MORB and within plate tholeiites; C, alkaline within-plate basalts; D, volcanic-arc basalts. Symbols are the same as in Fig. 3.

magmatism (e.g., Condie, 2005). In addition, the low La/Yb ratios (3.56–6.35 and 3.80–7.72) in both the quartz diorite and the basaltic andesite are indicative of such arc rocks (e.g., Hoffer et al., 2008).

Therefore, both the quartz diorite and the basaltic andesite formed in a continental arc above a convergent subduction zone.

The initial $^{87}Sr/^{86}Sr$ ratio and $\varepsilon_{Nd}(t)$ of both quartz diorite and basaltic andesite are plotted in the field of lithospheric mantle melting, similar to the Carboniferous basalts of the western Tianshan (Fig. 6). The $(Nb/Ta)_N$ ratios of quartz diorite and basaltic andesite are mostly <0.8, and the $(Zr/Hf)_N$ ratios are both about 1.0, indicating their enriched mantle source. Furthermore, the low La/Yb ratios (<7.80) and Nb/Y ratios (<0.30) for quartz diorite and basaltic andesite indicate that the metasomatic enrichment of the source regions was caused by a fluid derived from slab dehydration (e.g., Hoffer et al., 2008). This metasomatism explains the high concentrations of Rb, Ba, Sr, Th, U, K, La, and Ce in the subsequent melts.

As is shown on a Zr/Nb–Zr diagram (Geng et al., 2009), partial melting was associated with formation of the quartz diorite and the basaltic andesite, and the degree of melting for the generation of the quartz diorite was lower than that of the basaltic andesite (Fig. 7B). The partial melting trajectories that coincide with the quartz diorite and the basaltic andesite compositions imply >5% partial melting of an enriched mantle source based upon La abundance and La/Sm ratios (e.g., Green, 2006; Zhu et al., 2009) (Fig. 8A). The La/Sm and La/Yb ratios of the quartz diorite are 10.3–18.5 and 2.83–3.68, and the La/Sm and La/Yb ratios of the basaltic andesite are 9.95–16.9 and 2.82–3.72, which demonstrate that both the quartz diorite and the basaltic andesite originated by the batch partial melting of spinel peridotite (e.g., Genc and Tuysuz, 2010). In addition, the Dy/Yb ratio is an important geochemical index for distinguishing partial melting between the spinel and garnet stability fields of a phlogopite- and/or amphibole-bearing lherzolite (Duggen et al., 2005; Jiang et al., 2009). Partial melting in the garnet stability field generally leads to high Dy/Yb ratios (>2.5), whereas melting in the spinel stability field would produce melts with low Dy/Yb ratios (<1.5). Both the quartz diorite and the basaltic andesite have intermediate Dy/Yb ratios (1.59–1.81 and 1.70–1.82), which imply that the source mantle contains both garnet-facies and spinel-facies lherzolite. The Sm/Yb ratios of igneous rocks are sensitive to basalt source mineralogy, because Yb is typically more compatible in garnet than in clinopyroxene or spinel. The Yb concentrations and Sm/Yb ratios suggest that the mineral ratios of spinel/granet in the source region are all greater than 4. The degree of partial melting for the generation of both quartz diorite and basaltic andesite are about 10%, with that of the quartz diorite being slightly lower (Fig. 8B)

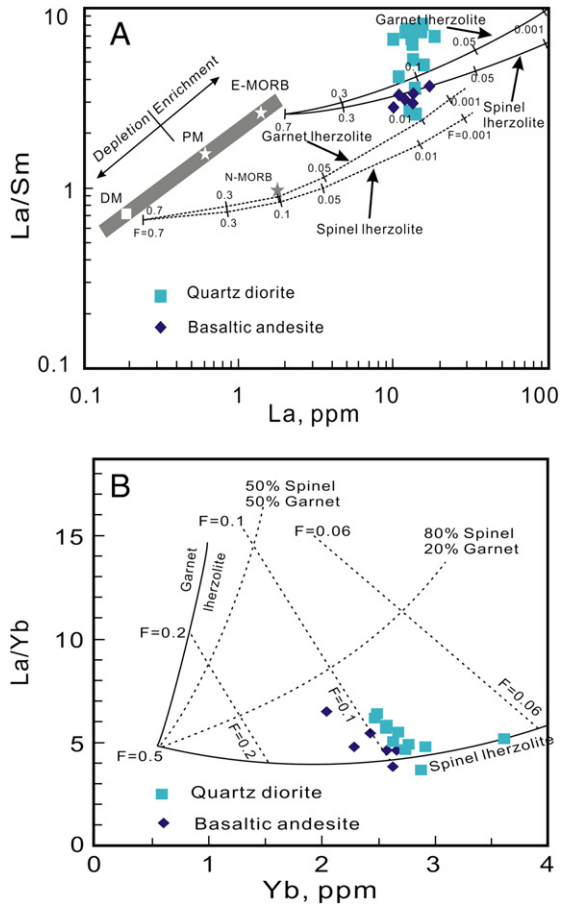

Fig. 8. Plot of La vs. La/Sm (A) and Yb vs. La/Yb (B) for the Late Paleozoic quartz diorite and basaltic andesite in the Yuximolegai area (for details, see Zhu et al., 2009).

5.2. The shoshonitic K-rich trachyandesite

The K-rich trachyandesite has some geochemical characteristics of mantle-derived shoshonitic rocks. Its higher Na_2O and K_2O contents and lower CaO and TiO_2 contents, as compared to the calc-alkaline rocks, are caused by the presence of alkali-feldspar and the lower An content of plagioclase. The Sr–Nd isotopic composition of the K-rich trachyandesite is similar to that of the quartz diorite and basaltic andesite, which is characteristic of a mantle derivation (Fig. 6). The Dy/Yb ratios of 1.61–1.89 suggest that it would be generated by the partial melting of both garnet-facies and spinel-facies lherzolite. The K-rich trachyandesite has variable Zr contents and concentrated Zr/Nb ratios, suggesting that fractional crystallization played a role in their petrogenesis (Fig. 7B), probably dominated by the fractional crystallization of clinopyroxene, hornblende, and plagioclase.

The K-rich trachyandesite is rich in Ba and Rb, which could have resulted from magma generation in a subduction zone, because Ba and Rb are highly incompatible LILE and can be mobilized during metamorphism and hydrothermal alteration (Arculus, 1994; Kawahata et al., 2001; Polat and Hofmann, 2003; Jenner et al., 2009). The variation of Ba/La and Rb/Yb ratios are positively correlated to K_2O contents in the K-rich trachyandesite (Fig. 9A and B). However, their correlation trends are different from those of the quartz diorite and basaltic andesite, implying differences in source materials (e.g., Jenner et al., 2009).

Geochemical studies of modern arc-related magmatism have shown that Ba/La can be used as an indicator of the total slab-derived input into the mantle wedge (Carr et al., 1990; Lin et al., 1990; Leeman et al., 1994; Patino et al., 2000; Jenner et al., 2009). Carr et al. (1990) observed that there is a correlation between Ba/La of arc lavas and subduction angle along the Central American arc. They attributed low Ba/La to metasomatism of a larger volume of the overlying mantle wedge during shallow subduction, resulting in a less pronounced subduction signature. The significantly higher Ba/La ratios of the K-rich trachyandesite imply that their generation is associated with the rollback of a subducting slab. The Ba/Nb ratio can be taken as an indicator of the amount of fluid in the mantle source region, or as a rough proxy for water content (Cervantes and Wallace, 2003).

The Ba/Nb ratios for the K-rich trachyandesite ranged from 73 to 450, which is higher than that of quartz diorite and basaltic andesite, suggesting that a considerable amount of hydrous minerals, amphiboles or phlogopites, existed in the source region. Amphiboles from mantle xenoliths display relatively high contents of K, Sr, LREE, HFSE, and, in some cases, Ba, but very low content of Rb and Th (Ionov and Hofmann, 1995; Chazot et al., 1996). In contrast, phlogopites are rich in K, Sr, Ba, and Rb, but have very low concentrations of REE, HFSE, and Th. The K/Rb ratios of phlogopites varied from 40 to 400, whereas those of amphiboles and amphibole-bearing melt are generally greater than 1100. The K-rich trachyandesite has relatively lower K/Rb ratios of 150–310, and REE and HFSE abundances, indicating that phlogopites are the dominant hydrous minerals in the source region. Phlogopites are stable at depths of more than 70 km

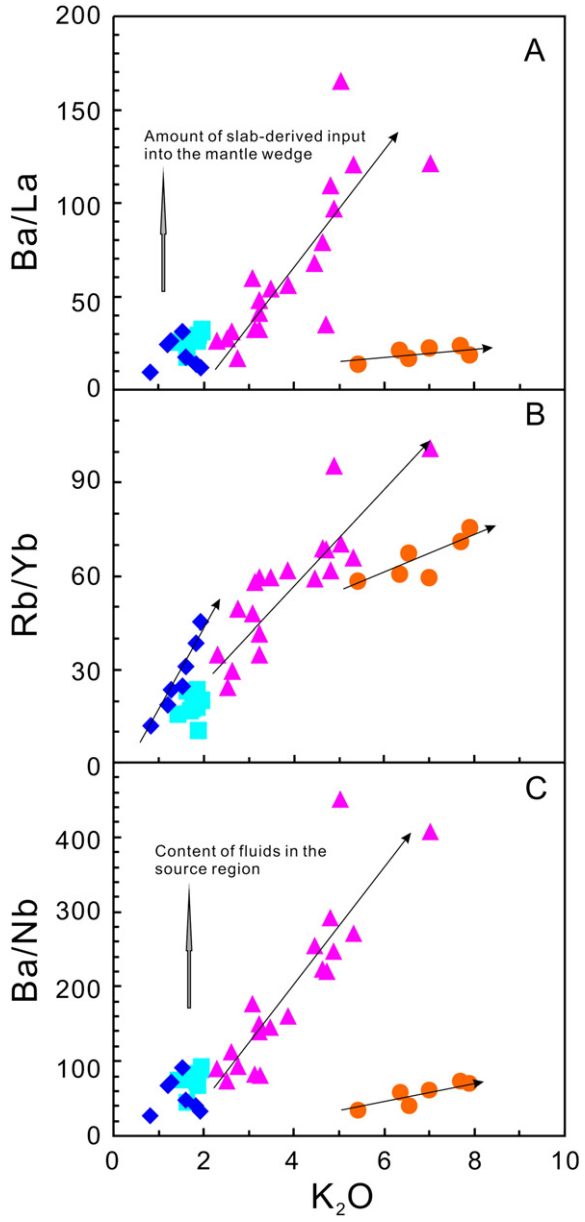

Fig. 9. Co-variation diagrams of Ba/La vs. K_2O (A), Rb/Yb vs. K_2O (B) and Ba/Nb vs. K_2O (C) for the igneous association in the Yuximolegai area, demonstrating the variations in these element ratios are a primary feature (Jenner et al., 2009). Symbols are the same as in Fig. 3.

(Chakrabarti et al., 2009), which suggests the primary magma of the K-rich trachyandesite in the Yuximolegai area was generated at great depth. Regionally, the K-rich trachyandesite and the ultrapotassic rocks at Bugula (Rb–Sr isochronal age of 294.0 ± 8.7 Ma: W-B Yang, unpub. data) have been regarded as co-magmatic intrusions into rocks of the Dahalajunshan Formation (Yang et al., 2010).

5.3. The quartz syenite porphyry

The quartz syenite porphyry is quite different from the three other igneous rocks described above, both in geochemical characteristics and in magma source. The Zr/Nb ratio of the quartz syenite porphyry increases as the Zr concentration increases (Fig. 7), suggesting magma generation during partial melting. The Ba/La and Ba/Nb ratios of the porphyry, as well as of the quartz diorite and the calc-alkaline basaltic andesite, are significantly lower than those of the K-rich trachyandesite. Furthermore, the correlation trends for Ba/La vs. K_2O, Rb/Yb vs. K_2O, and Ba/Nb vs. K_2O for the quartz syenite porphyry are different from those for the K-rich trachyandesite (Fig. 9). These geochemical characteristics indicate that the source regions for the quartz syenite porphyry and the K-rich trachyandesite are different (Fig. 9).

The quartz syenite porphyry has a lower $Mg^{\#}$ (18–33 ppm), higher La/Yb ratio, and more pronounced Eu depletion than the other igneous rocks, implying that it could be generated by the partial melting of a hot juvenile crust. Richards (2009) proposed that post-subduction arc contraction caused by collision may lead to crustal thickening and delamination of the subcontinental lithospheric mantle, with partial melting occurring in depressed lower crustal rocks as isotherms rebound or hot asthenospheric melts invade. The resulting magmas are more felsic, commonly with calc-alkaline to mildly alkaline character. Pe-Piper et al. (2009) proposed that the shoshonitic rocks (SiO_2 = 58.2–65.6%) from Limnos Island, Greece, are the products of partial melting of metabasalts in the lower crust. An experimental study showed that the K-rich syenitic/trachytic melts can be formed from low silica shoshonitic rocks, with SiO_2 of 54.2%, at 1050 °C and 1.5–2.5 GPa (Xiao and Clemens, 2007). Therefore, the quartz syenite porphyry in the Yuximolegai area is most likely derived from the partial melting of a post-subduction thickened crust or of hot juvenile basalt in the lower crust during mantle delamination in Early Permian. The Sr–Nd isotopic compositions ($(^{87}Sr/^{86}Sr)_i$ = 0.704110–0.706220, εNd(t) = 3.7–4.0) also indicate a depleted source, and suggest melts from a hot, juvenile lower crust (Geng et al., 2009).

5.4. Tectonic settings and geodynamic implications

Igneous rocks with geochemical signatures characteristic of volcanic arc magmatism are widely distributed in the western part of the

Table 4
A compilation of geochronological data of Late Carboniferous to Permian igneous rocks in Awulale and nearby districts.

Rocks	Localities	Age(Ma)	Methods	References
Basalt	Songhu	327.6 ± 2.2	Zircon U–Pb SIMS	Authors' unpublished data
Basalt	Laerdundaban	324.0 ± 4.9	Zircon U–Pb SHRIMP	Zhu et al. (2009)
Rhyolite	Chagangnuoer	319.2 ± 7.6	Zircon U–Pb	Authors' unpublished data
Rhyolite	Yuximolegai	316.0 ± 2.5	Zircon U–Pb SHRIMP	Zhu et al. (2009)
Trachy andesite	Laerdundaban	312.8 ± 4.2	Zircon U–Pb SHRIMP	Zhu et al. (2005)
Quartz diorite	Yuximolegai	310.8 ± 4.2	Zircon U–Pb SIMS	This study
Basalt	Nulasai	298 ± 7	Rb–Sr isochron	Li et al. (1997)
Shoshonite	Bugula	294.0 ± 8.7	Rb–Sr isochron	Authors' unpublished data
Shoshonite	Kezikezang	288 ± 6	Ar–Ar plateau	Zhao et al. (2009)
Quartz syenite porphyry	Yuximolegai	284.4 ± 4.0	Zircon U–Pb	This study
A-type granite	Kekesu	277 ± 3	Zircon U–Pb	Wang et al. (2009)
Rhyolite	Aikendaban	270.7 ± 1.3	Ar–Ar plateau	Chen et al. (2004b)
Adakite	Mosizaote	268 ± 5	Ar–Ar plateau	Zhao et al. (2009)
Rhyolite	Aikendaban	263.9 ± 7.0	Ar–Ar plateau	Chen et al. (2004b)
Adakite	Mosizaote	259.5 ± 0.5	Zircon U–Pb	Zhao et al. (2009)

Tianshan, and reflect subduction of the Paleozoic southern Tianshan ocean northward under the Kazakhstan–Yili plate or block (Gao and Klemd, 2000; Sun et al., 2008; Gao et al., 2009; Xiao et al., 2009, 2010a,b; Dong et al., 2011). The ages of the subduction-related igneous rocks became gradually younger from west to east, and they mainly formed in Late Carboniferous in the eastern Awulale Mountains, including in the Yuximolegai area (Zhu et al., 2009) (Table 4). After the closure of the southern Tianshan Ocean, final collision between the Tarim plate and the Kazakhstan–Yili plate occurred at ca. 300 Ma (Gao et al., 2009; Ren et al., 2011). Subsequent magmatism took place in an intraplate environment, perhaps associated with post-collisional transcurrent events (Wang et al., 2009).

Based on the geochemical and geochronological constraints of the Late Paleozoic igneous rocks from the Yuximolegai area, the Carboniferous and Permian evolution of the western Tianshan is shown in Fig. 10. Before ~310 Ma, subduction of the southern Tianshan Ocean slab was relatively flat because there is a less pronounced subduction signature in the associated calc-alkaline magmatic rocks. These include the quartz diorite (310.8 ± 2.1 Ma) and basaltic andesite in the Yuximolegai region and throughout the eastern end of the Kazakhstan–Yili plate.

After ~310 Ma, as a result of steepening of the slab during rollback, a series of phlogopite-bearing veins formed in the mantle wedge at depths of more than 70 km, which was the source for the K-rich trachyandesite parent magma. With the closure of the southern

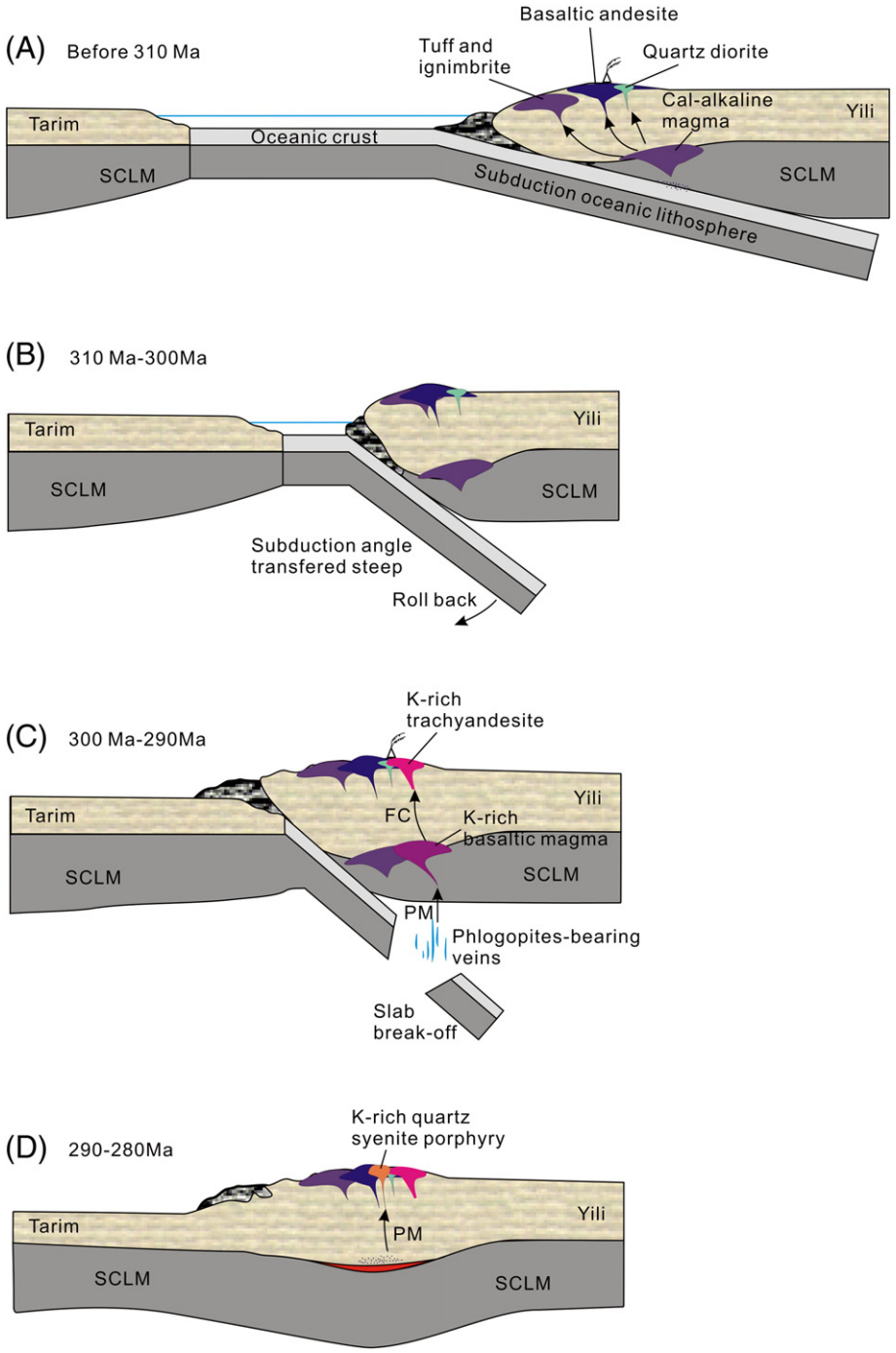

Fig. 10. Tectonic evolution model of the western Tianshan responsible for the Late Paleozoic igneous rocks in the Yuximolegai area. SCLM — subcontinental lithospheric mantle, FC — fractional crystallization, PM — partial melting. A: Normal arc magmatism before 310 Ma, induced by shallow plate subduction. B: The subduction angle transferred steep during 310 to 300 Ma. C: Slab break-off, phlogopite-bearing veins partially melted in the window wedge. D: Collisional lithospheric thickening.

Tianshan Ocean at ~300 Ma, the subducted slab below the western Tianshan may have broken off due to downward traction, and thus may have allowed even further asthenospheric interaction (e.g., Negrete-Aranda and Canon-Tapia, 2008). The flow of hot mantle material into the mantle wedge led to the partial melting of the wedge with its phlogopite-bearing veins to form the K-rich mafic magma responsible for the K-rich trachyandesite and the Bugula shoshonites that were generated by the fractional crystallization of pyroxene and plagioclase.

During the 290 Ma–280 Ma period, the hot juvenile basalt in the lower crust was partially melted to form the K-rich syenite magma (284.4 ± 4.0 Ma); melting was induced by collisional lithospheric thickening. Numerous Permian rhyolites, adakites and A-type granites (Table 4), associated with porphyry Cu (–Au) mineralization, are widespread in Awulale Mountains and western Tianshan (Wang et al., 2009; Zhao et al., 2009; and references within). It is suggested that post-collisional lithospheric mantle delamination and asthenospheric upwelling occurred after 280 Ma (e.g., Richards, 2009). Permian shoshonitic series volcanic rocks (SSVR) and adakites, with ages from 280 to 250 Ma, in the Awulale Mountains were described by Zhao et al. (2009). Interpretation of trace element, REE, and Sr–Nd isotopic compositions suggests that both SSVR and adakites possess similar source regions that contain underplated mantle-derived basaltic materials. Therefore, we can infer that the geodynamic setting of the western Tianshan was transformed to a post-subduction lithospheric extensional regime in Permian.

6. Conclusion

Late Paleozoic magmatism in Yuximolegai area, western Tianshan, is characterized by the transformation from Late Carboniferous calc-alkaline series that is characteristic of subduction-derived potassic igneous rocks, to Permian post-subduction related shoshonitic series. Igneous rocks are characterized by an enrichment in LILE and a depletion in HFSE, which is indicative of magmatism in an active continental margin environment. The age-corrected $\varepsilon Nd(t)$, ranging from $+2.3$ to $+5.5$, is consistent with magma derived from melting of lithospheric mantle. A tectonic transformation from low-angle subduction to steeper subduction, followed by slab break-off and crustal thickening, is proposed for the generation of the calc-alkaline and shoshonitic rocks in the Yuximolegai area from 310.8 ± 2.1 Ma to 284.4 ± 4.0 Ma.

Acknowledgments

We sincerely thank Professors Franco Pirajno, Fanrong Chen, Xingchun Zhang and an anonymous reviewer for their constructive and helpful reviews on this manuscript. We thank Dr. Rich Goldfarb for efficient editing and English polishing. We also appreciate the assistance of Ms. Hong Zhang, Guangqian Hu and Ying Liu, Mr. Xianglin Tu and Jinlong Ma, Dr. Xirong Liang and Qiuli Li, for geochemical and geochronological analyses. This research was financially supported by the Knowledge Innovation Program of Chinese Academy of Sciences (KZCX2-YW-107) and National Natural Science Foundation of China (41173040). This is GIGCAS contribution IS-1405.

References

Aldanmaz, E., Pearce, J.A., Thirlwall, M.F., Mitchell, J.G., 2000. Petrogenetic evolution of late Cenozoic, post-collision volcanism in western Anatolia, Turkey. Journal of Volcanology and Geothermal Research 102 (1–2), 67–95.

Altherr, R., Topuz, G., Siebel, W., Sen, C., Meyer, H.P., Satir, M., Lahaye, Y., 2008. Geochemical and Sr–Nd–Pb isotopic characteristics of Paleocene plagioleucitites from the Eastern Pontides (NE Turkey). Lithos 105 (1–2), 149–161.

Altunkaynak, S., 2007. Collision-driven slab breakoff magmatism in northwestern Anatolia, Turkey. Journal of Geology 115 (1), 63–82.

Altunkaynak, S., Dilek, Y., 2006. Timing and nature of postcollisional volcanism in western Anatolia and geodynamic implications. Geological Society of America Special Papers 409, 321–351.

Altunkaynak, S., Genc, S.C., 2008. Petrogenesis and time-progressive evolution of the Cenozoic continental volcanism in the Biga Peninsula, NW Anatolia (Turkey). Lithos 102 (1–2), 316–340.

Arculus, R.J., 1994. Aspects of magma genesis in arcs. Lithos 33 (1–3), 189–208.

Avanzinelli, R., Lustrino, M., Mattei, M., Melluso, L., Conticelli, S., 2009. Potassic and ultrapotassic magmatism in the circum-Tyrrhenian region: significance of carbonated pelitic vs. pelitic sediment recycling at destructive plate margins. Lithos 113 (1–2), 213–227.

Black, L.P., Kamo, S.L., Allen, C.M., Aleinikoff, J.N., Davis, D.W., Korsch, R.J., Foudoulis, C., 2003. TEMORA 1: a new zircon standard for Phanerozoic U–Pb geochronology. Chemical Geology 200 (1–2), 155–170.

Blatter, D.L., Carmichael, I.S.E., Deino, A.L., Renne, P.R., 2001. Neogene volcanism at the front of the central Mexican volcanic belt: basaltic andesites to dacites, with contemporaneous shoshonites and high-TiO_2 lava. Geological Society of America Bulletin 113 (10), 1324–1342.

Blatter, D.L., Carmichael, I.S.E., Deino, A.L., Renne, P., 2003. Discussion and reply: Neogene volcanism at the front of the central Mexican Volcanic Belt: basaltic andesites to dacites, with contemporaneous shoshonites and high-TiO_2 lava — reply. Geological Society of America Bulletin 115 (8), 1021–1024.

Boari, E., Tommasini, S., Laurenzi, M.A., Conticelli, S., 2009. Transition from ultrapotassic kamafugitic to sub-alkaline magmas: Sr, Nd, and Pb isotope, trace element and Ar-40–Ar-39 age data from the Middle Latin Valley Volcanic Field, Roman Magmatic Province, Central Italy. Journal of Petrology 50 (7), 1327–1357.

Bonin, B., 2004. Do coeval mafic and felsic magmas in post-collisional to within-plate regimes necessarily imply two contrasting, mantle and crustal, sources? A review. Lithos 78 (1–2), 1–24.

Boztug, D., et al., 2006. Geochemical characteristics of the composite Kaqkar batholith generated in a Neo-Tethyan convergence system, Eastern Pontides, Turkey. Journal of Asian Earth Sciences 27 (3), 286–302.

Callegari, E., Cigolini, C., Medeot, O., D'Antonio, M., 2004. Petrogenesis of calc-alkaline and shoshonitic post-collisional oligocene volcanics of the cover series of the Sesia Zone, western Italian Alps. Geodinamica Acta 17 (1), 1–29.

Carr, M.J., Feigenson, M.D., Bennett, E.A., 1990. Incompatible element and isotopic evidence for tectonic control of source mixing and melt extraction along the Central-American Arc. Contributions to Mineralogy and Petrology 105 (4), 369–380.

Cervantes, P., Wallace, P.J., 2003. Role of H_2O in subduction-zone magmatism: new insights from melt inclusions in high-Mg basalts from central Mexico. Geology 31 (3), 235–238.

Chakrabarti, R., Basu, A.R., Santo, A.P., Tedesco, D., Vaselli, O., 2009. Isotopic and geochemical evidence for a heterogeneous mantle plume origin of the Virunga volcanics, Western rift, East African Rift system. Chemical Geology 259 (3–4), 273–289.

Chazot, G., Menzies, M.A., Harte, B., 1996. Determination of partition coefficients between apatite, clinopyroxene, amphibole, and melt in natural spinel lherzolites from Yemen: implications for wet melting of the lithospheric mantle. Geochimica et Cosmochimica Acta 60 (3), 423–437.

Che, Z., Liu, L., Liu, H., Luo, J., 1996. Review on the ancient Yili rift, Xinjiang, China. Acta Petrologica Sinica 12 (3), 478–490 (in Chinese with English abstract).

Chen, Y.J., Bao, J.X., Zhang, Z.J., Liu, Y.L., Chen, H.Y., Cai, W.J., Helmstaedt, H., 2004a. Tectonic setting and element geochemistry of the Aikendaban formation volcanic rocks in west Tianshan. Journal of Mineralogy and Petrology 24 (3), 36–45 (in Chinese with English abstract).

Chen, Y.J., Liu, Y.L., Bao, J.X., Zhang, Z.J., Chen, H.Y., Cai, W.J., Helmstaedt, H., 2004b. Isotopic dating for the volcanic rocks of the Aikendaban formation in west Tianshan, China, and its tectonic implication. Journal of Mineralogy and Petrology 24 (1), 52–55 (in Chinese with English abstract).

Chen, J.L., Xu, J.F., Wang, B.D., Kang, Z.Q., Jie, L., 2010. Origin of Cenozoic alkaline potassic volcanic rocks at KonglongXiang, Lhasa terrane, Tibetan Plateau: products of partial melting of a mafic lower-crustal source? Chemical Geology 273 (3–4), 286–299.

Condie, K.C., 2005. High field strength element ratios in Archean basalts: a window to evolving sources of mantle plumes? Lithos 79 (3–4), 491–504.

Conticelli, S., Guarnieri, L., Farinelli, A., Mattei, M., Avanzinelli, R., Bianchini, G., Boari, E., Tommasini, S., Tiepolo, M., Prelevic, D., Venturelli, G., 2009a. Trace elements and Sr–Nd–Pb isotopes of K-rich, shoshonitic, and calc-alkaline magmatism of the Western Mediterranean Region: genesis of ultrapotassic to calc-alkaline magmatic associations in a post-collisional geodynamic setting. Lithos 107 (1–2), 68–92.

Conticelli, S., Marchionni, S., Rosa, D., Giordano, G., Boari, E., Avanzinelli, R., 2009b. Shoshonite and sub-alkaline magmas from an ultrapotassic volcano: Sr–Nd–Pb isotope data on the Roccamonfina volcanic rocks, Roman Magmatic Province, Southern Italy. Contributions to Mineralogy and Petrology 157 (1), 41–63.

Davies, J.H., Blanckenburg, F.V., 1995. Slab breakoff — a model of lithosphere detachment and its test in the magmatism and deformation of collisional orogens. Earth and Planetary Science Letters 129 (1–4), 85–102.

Dilek, Y., Altunkaynak, S., 2007. Cenozoic crustal evolution and mantle dynamics of post-collisional magmatism in western Anatolia. International Geology Review 49 (5), 431–453.

Dong, Y., Zhang, G., Neubauer, F., Liu, X., Hauzenberger, C., Zhou, D., Li, W., 2011. Syn- and post-collisional granitoids in the Central Tianshan orogen: geochemistry, geochronology and implications for tectonic evolution. Gondwana Research 20, 568–581.

Duggen, S., Hoernle, K., Van den Bogaard, P., Garbe-Schonberg, D., 2005. Post-collisional transition from subduction- to intraplate-type magmatism in the westernmost Mediterranean: evidence for continental-edge delamination of subcontinental lithosphere. Journal of Petrology 46 (6), 1155–1201.

Eyuboglu, E., Chung, S.-L., Santosh, M., Dudas, F.O., Akaryali, E., 2011. Transition from shoshonitic to adakitic magmatism in the eastern Pontides, NE Turkey: implications for slab window melting. Gondwana Research 19, 413–429.

Foley, S., 1992. Vein-plus-wall-rock melting mechanisms in the lithosphere and the origin of potassic alkaline magmas. Lithos 28 (3–6), 435–453.
Foley, S.F., Venturelli, G., Green, D.H., Toscani, L., 1987. The ultrapotassic rocks — characteristics, classification, and constraints for petrogenetic models. Earth-Science Reviews 24 (2), 81–134.
Gao, J., Klemd, R., 2000. Eclogite occurrences in the southern Tianshan high-pressure belt, Xinjiang, western China. Gondwana Research 3, 33–38.
Gao, J., Long, L.L., Klemd, R., Qian, Q., Liu, D.Y., Xiong, X.M., Su, W., Liu, W., Wang, Y.T., Yang, F.Q., 2009. Tectonic evolution of the South Tianshan orogen and adjacent regions, NW China: geochemical and age constraints of granitoid rocks. International Journal of Earth Sciences 98 (6), 1221–1238.
Genc, S.C., Tuysuz, O., 2010. Tectonic setting of the Jurassic bimodal magmatism in the Sakarya Zone (Central and Western Pontides), Northern Turkey: a geochemical and isotopic approach. Lithos 118 (1–2), 95–111.
Geng, H.Y., Sun, M., Yuan, C., Xiao, W.J., Xian, W.S., Zhao, G.C., Zhang, L.F., Wong, K., Wu, F.Y., 2009. Geochemical, Sr–Nd and zircon U–Pb–Hf isotopic studies of Late Carboniferous magmatism in the West Junggar, Xinjiang: implications for ridge subduction? Chemical Geology 266 (3–4), 364–389.
Gill, R.C.O., Aparicio, A., El Azzouzi, M., Hernandez, J., Thirlwall, M.F., Bourgois, J., Marriner, G.F., 2004. Depleted arc volcanism in the Alboran Sea and shoshonitic volcanism in Morocco: geochemical and isotopic constraints on Neogene tectonic processes. Lithos 78 (4), 363–388.
Green, N.L., 2006. Influence of slab thermal structure on basalt source regions and melting conditions: REE and HFSE constraints from the Garibaldi volcanic belt, northern Cascadia subduction system. Lithos 87 (1–2), 23–49.
Hoffer, G., Eissen, J.P., Beate, B., Bourdon, E., Fornari, M., Cotten, J., 2008. Geochemical and petrological constraints on rear-arc magma genesis processes in Ecuador: the Puyo cones and Mera lavas volcanic formations. Journal of Volcanology and Geothermal Research 176 (1), 107–118.
Hong, D.W., Wang, S.G., Xie, X.L., Zhang, J.S., Wang, T., 2003. Metallogenic province derived from mantle sources: Nd, Sr, S and Pb isotope evidence from the Central Asian Orogenic Belt. Gondwana Research 6, 711–728.
Hou, Z.Q., Xie, Y.L., Xu, W.Y., Li, Y.Q., Zhu, X.K., Khin, Z., Beaudoin, G., Rui, Z.Y., Wei, H.A., Ciren, L., 2007. Yulong deposit, eastern Tibet: a high-sulfidation Cu–Au porphyry copper deposit in the eastern Indo–Asian collision zone. International Geology Review 49 (3), 235–258.
Hu, A.Q., Wei, G.J., Zhang, J.B., Deng, W.F., Chen, L.L., 2008. SHRIMP U–Pb ages for zircons of the amphibolites and tectonic evolution significance from the Wenquan domain in the West Tianshan Mountains, Xinjiang, China. Acta Petrologica Sinica 24 (12), 2731–2740 (in Chinese with English abstract).
Ionov, D.A., Hofmann, A.W., 1995. Nb–Ta-rich mantle amphiboles and micas — implications for subduction-related metasomatic trace-element fractionations. Earth and Planetary Science Letters 131 (3–4), 341–356.
Irvine, T.N., Baragar, W.R.A., 1971. Guide to chemical classification of common volcanic rocks. Canadian Journal of Earth Sciences 8 (5), 523–548.
Jenner, F.E., Bennett, V.C., Nutman, A.P., Friend, C.R.L., Norman, M.D., Yaxley, G., 2009. Evidence for subduction at 3.8 Ga: geochemistry of arc-like metabasalts from the southern edge of the Isua Supracrustal Belt. Chemical Geology 261 (1–2), 82–97.
Jiang, C.Y., Wu, W., Zhang, X., Cui, S., 1995. The change from island arc to rift valley — evidence from volcanic rocks in Awulale area. Acta Petrologica et Mineralogica 14 (4), 289–300 (in Chinese with English abstract).
Jiang, C.Y., Wu, W., Zhang, X., Cui, S., 1996. Magma action and tectonic evolution in Awulale district, western Tianshan mountain. Journal of Xi'An College of Geology 18 (2), 18–25 (in Chinese with English abstract).
Jiang, Y.H., Jiang, S.Y., Ling, H.F., Dai, B.Z., 2006. Low-degree melting of a metasomatized lithospheric mantle for the origin of Cenozoic Yulong monzogranite-porphyry, east Tibet: geochemical and Sr–Nd–Pb–Hf isotopic constraints. Earth and Planetary Science Letters 241 (3–4), 617–633.
Jiang, Y.H., Jiang, S.Y., Dai, B.Z., Liao, S.Y., Zhao, K.D., Ling, H.F., 2009. Middle to late Jurassic felsic and mafic magmatism in southern Hunan province, southeast China: implications for a continental arc to rifting. Lithos 107 (3–4), 185–204.
Kawahata, H., Nohara, M., Ishizuka, H., Hasebe, S., Chiba, H., 2001. Sr isotope geochemistry and hydrothermal alteration of the Oman ophiolite. Journal of Geophysical Research-Solid Earth 106 (B6), 11083–11099.
Keto, L.S., Jacobsen, S.B., 1987. Nd and Sr isotopic variations of early paleozoic oceans. Earth and Planetary Science Letters 84, 27–41.
Koprubasi, N., Aldanmaz, E., 2004. Geochemical constraints on the petrogenesis of cenozoic I-type granitoids in northwest Anatolia, Turkey: evidence for magma generation by lithospheric delamination in a post-collisional setting. International Geology Review 46 (8), 705–729.
Leeman, W.P., Carr, M.J., Morris, J.D., 1994. Boron geochemistry of the Central-American Volcanic Arc — constraints on the genesis of subduction-related magmas. Geochimica et Cosmochimica Acta 58 (1), 149–168.
Li, X.H., 1997. Geochemistry of the Longsheng Ophiolite from the southern margin of Yangtze Craton, SE China. Geochemical Journal 31 (5), 323–337.
Li, H.Q., Zhou, S., Cai, H., 1997. Chronology of mineralization of the Nileike copper deposit in northern Xinjian. Acta Geoscientia Sinica 18, 185–187 (in Chinese with English abstract).
Li, X.H., Liu, D.Y., Sun, M., Li, W.X., Liang, X.R., Liu, Y., 2004. Precise Sm–Nd and U–Pb isotopic dating of the supergiant Shizhuyuan polymetallic deposit and its host granite, SE China. Geological Magazine 141 (2), 225–231.
Liang, H.Y., Campbell, I.H., Allen, C., Sun, W.D., Liu, C.Q., Yu, H.X., Xie, Y.W., Zhang, Y.Q., 2006. Zircon Ce^{4+}/Ce^{3+} ratios and ages for Yulong ore-bearing porphyries in eastern Tibet. Mineralium Deposita 41 (2), 152–159.
Liang, H.Y., Sun, W.D., Su, W.C., Zartman, R.E., 2009a. Porphyry copper–gold mineralization at Yulong, China, promoted by decreasing redox potential during magnetite alteration. Economic Geology 104 (4), 587–596.
Liang, J.L., Ding, X., Sun, X.M., Zhang, Z.M., Zhang, H., Sun, W.D., 2009b. Nb/Ta fractionation observed in eclogites from the Chinese Continental Scientific Drilling Project. Chemical Geology 268 (1–2), 27–40.
Lin, P.N., Stern, R.J., Morris, J., Bloomer, S.H., 1990. Nd-isotopic and Sr-isotopic compositions of lavas from the Northern Mariana and Southern Volcano Arcs — implications for the origin of island-arc melts. Contributions to Mineralogy and Petrology 105 (4), 381–392.
Ludwig, K.R., 2003. User's manual for Isoplot 3.0: a geolocronolgical toolkit for Microsoft Excel. Berkeley Geochronlogical Center Special Publication 4, 1–70.
Lugmair, G.W., Marti, K., 1978. Lunar initial 143Nd/144Nd: differential evolution of the lunar crust and mantle. Earth and Planetary Science Letters 39, 349–357.
Luo, Y., Niu, H.C., Shan, Q.A., Yang, W.B., Zhang, B., Zhou, C.P., Liao, S.P., Yu, X.Y., 2010. Geochemical characteristics and petrogenesis of the Aikendaban Permian shoshonite in the western Tianshan. Acta Petrologica Sinica 26 (10), 2925–2934 (in Chinese with English abstract).
Middlemost, E.A.K., 1994. Naming materials in the magma igneous rock system. Earth-Science Reviews 37 (3–4), 215–224.
Muller, D., Groves, D.I., 1993. Direct and indirect associations between potassic igneous rocks, shoshonites and gold–copper deposits. Ore Geology Reviews 8 (5), 383–406.
Muller, D., Groves, D.I., 1997. Potassic igneous rocks and associted gold–copper mineralization. Lecture Notes in Earth Sciences 56.
Muller, D., Rock, N.M.S., Groves, D.I., 1992. Geochemical discrimination between shoshonitic and potassic volcanic-rocks in different tectonic settings — a pilot-study. Mineralogy and Petrology 46 (4), 259–289.
Muller, D., Franz, L., Herzig, P.M., Hunt, S., 2001. Potassic igneous rocks from the vicinity of epithermal gold mineralization, Lihir Island, Papua New Guinea. Lithos 57 (2–3), 163–186.
Negrete-Aranda, R., Canon-Tapia, E., 2008. Post-subduction volcanism in the Baja California Peninsula, Mexico: the effects of tectonic reconfiguration in volcanic systems. Lithos 102 (1–2), 392–414.
Ni, S.B., Man, F.S., Chen, J.F., 1995. REE and Sr–Nd isotopic study of Qiongawuzi ultramafic intrusion, West Tianshan. Acta Petrologica Sinica 11 (1), 65–70 (in Chinese with English abstract).
Niu, H.C., Shan, Q.A., Luo, Y., Yang, W.B., Zhou, C.P., Liao, S.P., Yu, X.Y., 2010. Geochronological and geochemical studies on quartz diorite in Yuximolegai Daban, West Tianshan and its tectonic implication. Acta Petrologica Sinica 26 (10), 2935–2945 (in Chinese with English abstract).
Patino, L.C., Carr, M.J., Feigenson, M.D., 2000. Local and regional variations in Central American arc lavas controlled by variations in subducted sediment input. Contributions to Mineralogy and Petrology 138 (3), 265–283.
Pearce, J.A., 1982. Trace element characteristics of lavas from destructive plate boundaries. In: Thorps, R.S. (Ed.), Andesites. Wiley, Chichester, pp. 525–548.
Peccerillo, A., Taylor, S.R., 1976. Geochemistry of Eocene calc-alkaline volcanic-Rocks from Kastamonu area, Northern Turkey. Contributions to Mineralogy and Petrology 58 (1), 63–81.
Pe-Piper, G., Piper, D.J.W., Koukouvelas, I., Dolansky, L.M., Kokkalas, S., 2009. Post-orogenic shoshonitic rocks and their origin by melting underplated basalts: the Miocene of Limnos, Greece. Geological Society of America Bulletin 121 (1–2), 39–54.
Polat, A., Hofmann, A.W., 2003. Alteration and geochemical patterns in the 3.7–3.8 Ga Isua Greenstone Belt, West Greenland. Precambrian Research 126 (3–4), 197–218.
Qian, Q., Gao, J., Xiong, X.M., Long, L.L., Huang, D.Z., 2006. Petrogenesis and tectonic settings of Carboniferous volcanic rocks from north Zhaosu, western Tianshan Mountains: constraints from petrology and geochemistry. Acta Petrologica Sinica 22 (5), 1307–1323 (in Chinese with English abstract).
Ren, R., Han, B.F., Ji, J.Q., Zhang, L., Xu, Z., Su, L., 2011. U–Pb age of detrital zircons from the Tekes River, Xinjiang, China, and implications for tectonomagmatic evolution of the South Tian Shan Orogen. Gondwana Research 19, 460–470.
Richards, J.P., 2009. Postsubduction porphyry Cu–Au and epithermal Au deposits: products of remelting of subduction-modified lithosphere. Geology 37 (3), 247–250.
Rottura, A., Bargossi, G.M., Caggianelli, A., Del Moro, A., Visona, D., Tranne, C.A., 1998. Origin and significance of the Permian high-K calc-alkaline magmatism in the central-eastern Southern Alps, Italy. Lithos 45 (1–4), 329–348.
Seghedi, I., Downes, H., Szakacs, A., Mason, P.R.D., Thirlwall, M.F., Rosu, E., Pecskay, Z., Marton, E., Panaiotu, C., 2004. Neogene–Quaternary magmatism and geodynamics in the Carpathian–Pannonian region: a synthesis. Lithos 72 (3–4), 117–146.
Shan, Q., Zhang, B., Luo, Y., Zhou, C.P., Yu, X.Y., Zeng, Q.S., Yang, W.B., Niu, H.C., 2009. Characteristics and trace element geochemistry of pyrite from the Songhu iron deposit, Nilek County, Xinjiang, China. Acta Petrologica Sinica 25 (6), 1456–1464 (in Chinese with English abstract).
Steiger, R.H., Jäger, E., 1977. Subcommission on geochronology: convention on the use of decay constants in geo- and cosmochronology. Earth and Planetary Science Letters 36, 359–362.
Su, B.X., Qin, K.Z., Sakyi, P.A., Li, X.-H., Li, X.H., Yang, Y.H., Sun, H., Tang, D.M., Liu, P.P., Xiao, Q.H., Malaviarachchi, S.P.K., 2011. U–Pb ages and Hf–O isotopes of zircons from Late Paleozoic mafic–ultramafic units in the southern Central Asian Orogenic Belt: tectonic implications and evidence for an Early-Permian mantle plume. Gondwana Research 20, 516–531.
Sun, S.S., McDonough, W.F., 1989. Chemical and isotopic systematics of oceanic basalts: implications for mantle composition and process. In: Saunders, A.D., Norry, M.J. (Eds.), Magmatism in Oceanic Basins Geological Society London Special Publication, 42, pp. 313–345.

Sun, L.H., Wang, Y.J., Fan, W.M., Zi, J.W., 2008. Post-collisional potassic magmatism in the Southern Awulale Mountain, western Tianshan Orogen: petrogenetic and tectonic implications. Gondwana Research 14, 383–394.

Tang, G.J., Wang, Q., Wyman, D.A., Li, Z.X., Zhao, Z.H., Jia, X.H., Jiang, Z.Q., 2010. Ridge subduction and crustal growth in the Central Asian Orogenic Belt: evidence from Late Carboniferous adakites and high-Mg diorites in the western Junggar region, northern Xinjiang (west China). Chemical Geology 277 (3–4), 281–300.

Tu, X.L., Zhang, H., Deng, W.F., Ling, M.X., Ying, L.H., Liu, Y., Sun, W.D., 2011. Application of resolution in-situ laser ablation ICP-MS in trace element analyses. Geochimica 40 (1), 83–98 (in Chinese with English abstract).

Wang, B., Cluzel, D., Shu, L.S., Faure, M., Charvet, J., Chen, Y., Meffre, S., de Jong, K., 2009. Evolution of calc-alkaline to alkaline magmatism through Carboniferous convergence to Permian transcurrent tectonics, western Chinese Tianshan. International Journal of Earth Sciences 98, 1275–1298.

Wang, B., Shu, L.S., Faure, M., Jahn, B.M., Cluzel, D., Charvet, J., Chung, S.L., Meffre, S., 2011. Paleozoic tectonics of the southern Chinese Tianshan: insights from structural, chronological and geochemical studies of the Heiyingshan ophiolitic melange (NW China). Tectonophysics 497 (1–4), 85–104.

Wei, G.J., Liang, X.R., Li, X.H., Liu, Y., 2002. Precise measurement of Sr isotopic compositions of liquid and solid base using (LP) MCICP-MS. Geochimica 31 (3), 295–305 (in Chinese with English abstract).

Wood, D.A., 1980. The application of a Th–Hf–Ta diagram to problems of tectonomagmatic classification and to establishing the nature of crustal contamination of basaltic lavas of the British Tertiary Volcanic Province. Earth and Planetary Science Letters 50 (1), 11–30.

Xia, L., Zhang, G., Xia, Z., Xu, X., Dong, Y., Li, X., 2002. Constraints on the timing of opening and closing of the Tianshan Paleozoic oceanic basin: Evidence from Sinian and Carboniferous volcanic rocks. Geological Bulletin of China 21, 55–62 (in Chinese with English abstract).

Xia, L., Xia, Z., Xu, X., Li, X., Ma, Z., Wang, L., 2004. Carboniferous Tianshan ignous megaprovince and mantle plume. Geological Bulletin of China 23, 903–910 (in Chinese with English abstract).

Xiao, L., Clemens, J.D., 2007. Origin of potassic (C-type) adakite magmas: experimental and field constraints. Lithos 95 (3–4), 399–414.

Xiao, W.J., Kusky, T., 2009. Geodynamic processes and metallogenesis of the Central Asian and related orogenic belts: introduction. Gondwana Research 16, 167–169.

Xiao, W.J., Windley, B.F., Huang, B.C., Han, C.M., Yuan, C., Chen, H.L., Sun, M., Sun, S., Li, J.L., 2009. End-Permian to mid-Triassic termination of the accretionary processes of the southern Altaids: implications for the geodynamic evolution, Phanerozoic continental growth, and metallogeny of Central Asia. International Journal of Earth Sciences 98, 1189–1217.

Xiao, W.J., Han, C.M., Yuan, C., Sun, M., Zhao, G.C., Shan, Y.H., 2010a. Transitions among Mariana-, Japan-, Cordillera- and Alaska-type arc systems and their final juxtapositions leading to accretionary and collisional orogenesis. Geological Society, London, Special Publications 338, 35–53.

Xiao, W.J., Huang, B.C., Han, C.M., Sun, S., Li, J.L., 2010b. A review of the western part of the Altaids: a key to understanding the architecture of accretionary orogens. Gondwana Research 18, 253–273.

Xiong, X.L., Zhao, Z.H., Bai, Z.H., Mei, H.J., Xu, J.F., Wang, Q., 2001. Origin of Awulale adakitic sodium-rich rocks in western Tianshan: constraints for Nd and Sr isotopic compositions. Acta Petrologica Sinica 17 (4), 514–522 (in Chinese with English abstract).

Yang, W.B., Niu, H.C., Luo, Y., Shan, Q.A., Zhou, C.P., Liao, S.P., Yu, X.Y., 2010. Ar-40/Ar-39 age and geochemistry of the ultrapotassic magmatic rocks from Bugula in Nileke, Xinjiang and its tectonic implication. Acta Petrologica Sinica 26 (10), 3065–3073 (in Chinese with English abstract).

Zhang, M., O'Reilly, S.Y., 1997. Multiple sources for basaltic rocks from Dubbo, eastern Australia: geochemical evidence for plume lithospheric mantle interaction. Chemical Geology 136 (1–2), 33–54.

Zhang, D.Y., Zhang, Z.C., Ai, Y., Su, H.M., 2009. Geochronology, geochemistry of the oresbearing porphyries in the Lailisigao'er region, western Tianshan: implications for their tectonic setting and mineralization. Acta Petrologica Sinica 25 (6), 1319–1331 (in Chinese with English abstract).

Zhang, D.Y., Zhang, Z.C., Xue, C.J., Ai, Y., 2010. Petrology and geochemistry of the oreforming porphyries in the Lamasu copper deposit, western Tianshan: implications for petrogenesis. Acta Petrologica Sinica 26 (3), 680–694 (in Chinese with English abstract).

Zhao, Z.H., Bai, Z.H., Rui, Z.Y., Xiong, X.L., Mei, H.J., Wang, L.S., Wang, Y.X., Bao, Z.W., 2000. Forecasting map of igneous rocks and mineralization in northern Western Tianshan. Project reports of "Late Paleozoic volcanisms, shallow intrusive magmatism and Cu–Au polymetallic mineralization studies in northern West Tianshan". . (In Chinese).

Zhao, Z.H., Xiong, X.L., Wang, Q., Bai, Z.H., Xu, J.F., Qiao, Y.L., 2004. Association of late paleozoic adakitic rocks and shoshonitic volcanic rocks in the western Tianshan, China. Acta Geologica Sinica — English Edition 78 (1), 68–72.

Zhao, Z.H., Xiong, X.L., Wang, Q., Bai, Z.H., Qiao, Y.L., 2009. Late Paleozoic underplating in North Xinjiang: evidence from shoshonites and adakites. Gondwana Research 16 (2), 216–226.

Zhu, Y.F., Zhang, L.F., Gu, L.B., Guo, X., Zhou, J., 2005. The zircon SHRIMP chronology and trace element geochemistry of the Carboniferous volcanic rocks in western Tianshan Mountains. Chinese Science Bulletin 50 (19), 2201–2212.

Zhu, Y.F., Zhou, J., Guo, X.A., 2006a. Petrology and Sr–Nd isotopic geochemistry of the Carboniferous volcanic rocks in the western Tianshan Mountains, NW China. Acta Petrologica Sinica 22 (5), 1341–1350 (in Chinese with English abstract).

Zhu, Y.F., Zhou, J., Song, B., Zhang, L.F., Guo, X., 2006b. Age of the "Dahalajunshan" Formation in Xinjiang and its disintegration. Geology in China 33 (3), 488–498 (in Chinese with English abstract).

Zhu, Y.F., Guo, X., Song, B., Zhang, L.F., Gu, L.B., 2009. Petrology, Sr–Nd–Hf isotopic geochemistry and zircon chronology of the Late Palaeozoic volcanic rocks in the southwestern Tianshan Mountains, Xinjiang, NW China. Journal of the Geological Society 166, 1085–1099.

Zuo, G., Zhang, Z., Wang, Z., Liu, M., Wang, L., 2008. Tectonic division, stratigraphical stystem and the evolution of western Tianshan Mountains. Xinjiang. Geological Review 54, 748–767 (in Chinese with English abstract).